

Constitutive Modeling and Application of Finite Element Analysis in Geotechnical Engineering*

A. Varadarajan†

Introduction

Geotechnical materials range from rock to clay. Their behaviour is complex and is affected by such factors as the geologic history of formation, environmental factors, stress history, drainage condition and stress-path. Testing of these materials in the laboratory and in the field to understand their behaviour has been a challenging task to geotechnical engineers. Direct shear tests, triaxial shear tests, ring shear tests and cubical or multiaxial tests are among the different tests used in the laboratory. Specialized tests to capture strain softening behaviour and large sized particles are also used.

The constitutive models that are used to characterise the behaviour of geologic materials include primarily linear elastic, nonlinear elastic, elastoplastic and elastoviscoplastic models. The development of constitutive models have assumed considerable importance in recent times due to the emergence of powerful numerical methods. The numerical methods such as Finite Element Method, FEM and Boundary Element Method, BEM, have revolutionised the ability to predict the behaviour of various engineering systems in general and geotechnical engineering problems in particular.

In this presentation, the objectives are (i) to discuss the constitutive models used to characterise the behaviour of geologic materials and testing of geologic materials to determine material parameters and to verify the models and (ii) analysis of various engineering problems using finite element method with various constitutive models. The contents of the presentation are primarily those with which the author has been associated with over the years.

* 24th Annual Lecture delivered at IGC-2001, Indore.

† Professor, Department of Civil Engineering, Indian Institute of Technology Delhi, New Delhi - 110 016.

Constitutive Modeling and Testing

The constitutive models considered include hyperbolic model, hierarchical single surface model and the model based on disturbed state concept. Testing of geologic materials with stress controlled triaxial tests, computer controlled triaxial tests, multiaxial tests, large size triaxial tests under high stresses and servo-controlled triaxial tests under high stresses are discussed. The materials tested include, clay, reinforced sand, rock salt, rock-fill material and rock.

Hyperbolic Model

The simplest constitutive law, which is used for geologic materials is the linear elastic stress-strain equation based on Hooke's law. The non-linearity of the stress-strain relationship observed in the case of soils is commonly expressed using hyperbola proposed by Kondner and Zelasko (1963). It is expressed as (Fig.1)

$$(\sigma_1 - \sigma_3) = \frac{\varepsilon_1}{a + b\varepsilon_1} \quad (1)$$

where $(\sigma_1 - \sigma_3)$ = deviator stress

ε_1 = axial strain

a, b = constants

$$a = \frac{1}{E_i}$$

E_i = initial tangent modulus

$$b = \frac{1}{(\sigma_1 - \sigma_3)_{ult}}$$

$(\sigma_1 - \sigma_3)_{ult}$ = asymptotic value of the deviator stress.

The stress-strain relationships of soils were found to be dependent on stress-path when tested under drained condition, (Yudhbir and Varadarajan, 1975). The stress-path dependent behaviour was determined by applying stress-controlled loading during shearing stage of the triaxial test. A hanger system with lever arrangement was used in the test. Increments of loading and variable cell pressure were applied to follow a predetermined stress-path. Drained triaxial tests were conducted on normally consolidated Rann of Kutch clay (LL = 91%, PI = 49%) using four stress-paths; stress-path A in which axial stress, σ_1 , was increased keeping lateral stress σ_3 constant, stress-path B

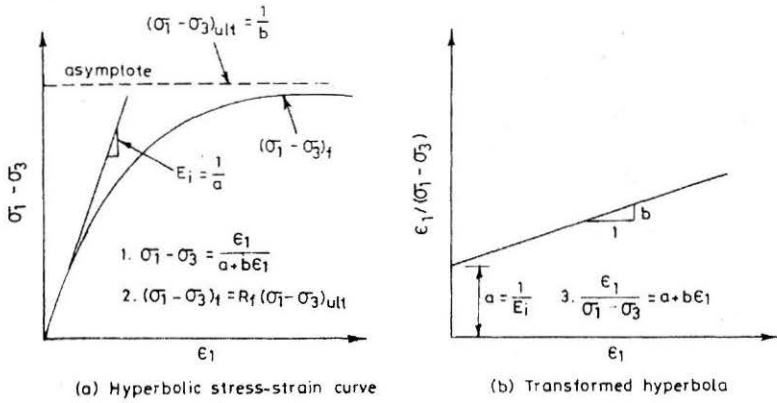


FIGURE 1 : Hyperbolic Representation of Stress-Strain Curve

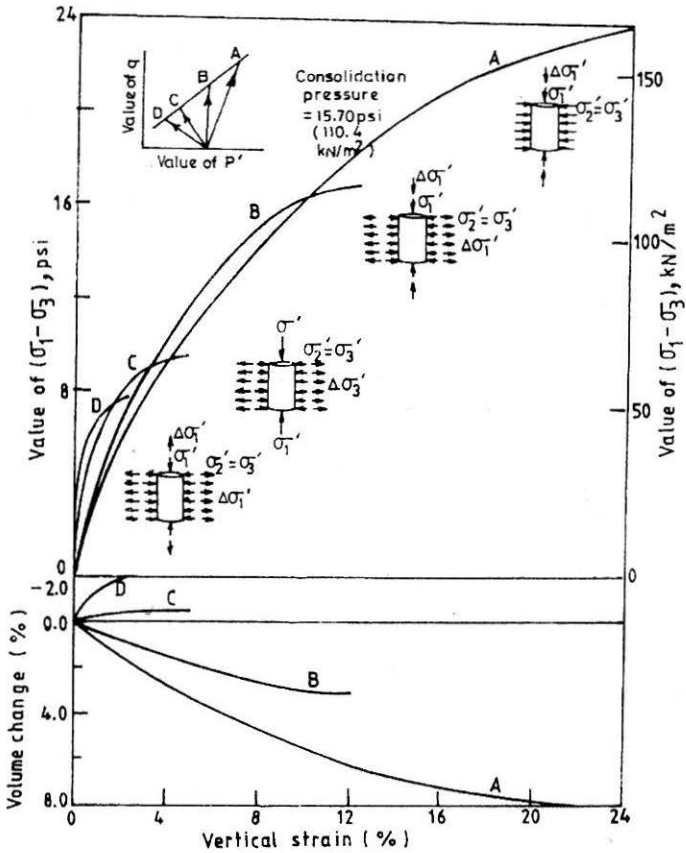


FIGURE 2 : Stress-Strain Volume Change Behaviour of A Normally Consolidated Clay under Various Stress-Paths

in which σ_3 was decreased and σ_1 was increased such that $(\sigma_1 + 2\sigma_3)/3$ was constant, stress-path C, in which σ_3 was decreased keeping σ_1 constant and stress-path D, in which σ_1 and σ_3 were decreased such that $\Delta\sigma_1/\Delta\sigma_3 = 0.4$. The stress-strain volume change behaviour of these stress-path tests are shown in Fig.2. Various stress-path tests were conducted on three types of sands, which were isotropically and anisotropically consolidated samples (Mishra, 1981). It was found that the modulus values were dependent on stress-path, but the strength parameters were independent of stress-path. Using the hyperbolic model, stress-path dependent behaviour of the stress-strain relationship was presented (Varadarajan and Yudhbir, 1975; Arora, 1980; Mishra, 1981).

Hierarchical Single Surface Model

Features of the Model

Hierarchical single surface (HISS) model is an elastoplastic constitutive model. In the HISS model a unified or hierarchical approach is adopted in the development to systematically include responses of progressive complexities such as isotropic hardening with associative flow rule and isotropic hardening with non-associative flow rule (Desai et al., 1986). This approach also enables simplification in the determination of material constants from laboratory tests and the number of constants as well. The continuous yielding and ultimate yield behaviour is given by a compact and specialised form of the general polynomial representation as

$$F = \frac{J_{2D}}{P_a^2} - \left[-\alpha \left(\frac{J_1}{P_a} \right)^n + \gamma \left(\frac{J_1}{P_a} \right)^2 \right] (1 - \beta S_r)^m = 0 \quad (2)$$

$$\text{or } F = \bar{J}_{2D} - F_b F_s = 0 \quad (3)$$

where J_{2D} is the second invariant of the deviatoric stress tensor, J_1 , is the first invariant of stress tensor, $\bar{J}_{2D} = J_{2D}/P_a^2$, P_a is the atmospheric pressure, α , β and m are material response functions associated with the ultimate behaviour, α is the hardening function, n is the phase change parameter and S_r is the ratio given by

$$S_r = \frac{\sqrt{27} J_{3D}}{2 J_{2D}^{1.5}} \quad (4)$$

in which J_{3D} is the third invariant of deviator stress tensor. In Eqn.(3) F_b is

the basic function describing the shape of the yield function in $J_1 - \sqrt{J_{2D}}$ plane and F_s is the shape function which describes the shape in the octahedral plane.

The hardening function, α is given by

$$\alpha = \frac{a_1}{\xi^{\eta_1}} \quad (5)$$

where a_1 and η_1 are the hardening parameters, and $\xi = \int (d\varepsilon_{ij}^p d\varepsilon_{ij}^p)^{1/2}$ is the trajectory of the plastic strains.

For the non-associative plasticity, the plastic potential function, Q is defined as

$$Q = \frac{J_{2D}}{P_a^2} \left[-\alpha_Q \left(\frac{J_1}{P_a} \right)^n + \gamma \left(\frac{J_1}{P_a} \right)^2 \right] F_s \quad (6)$$

where $\alpha_Q = \alpha + \kappa(\alpha_0 - \alpha)(1 - r_v)$ (7)

in which $r_v = \xi_v / \xi$ and ξ_v is the volumetric part of ξ , α_0 is the value of α at the end of initial hydrostatic loading and κ is the non-associative parameter.

Determination of Material Parameters

The procedure for the determination of material parameters has been described in detail in various references (for example, Desai and Wathugala, 1987 and Varadarajan and Desai, 1993). It is briefly presented in the following:

At ultimate condition, the hardening function, α is zero and F can be arranged as

$$\left[\frac{J_{2D}}{J_1^2} \right]^{1/m} \gamma^{1/m} + \beta S_r = 1 \quad (8)$$

The value of m is found to be -0.5 for geologic materials. The values of γ and β are determined using ultimate stresses from various stress path tests.

The value of phase change parameter, n is determined at the state of stress at which the plastic volume change is zero. At this condition,

$$n = \frac{2}{1 - \left(\frac{J_{2D}}{J_1^2} \right) \cdot \left(\frac{1}{F_s \gamma} \right)} \quad (9)$$

The value of n is obtained by averaging the values obtained from various tests.

The hardening parameters a_1 and η_1 are determined using Eqn.(5) from known α and ξ values at various stress levels of a test. The value of α is calculated by rearranging Eqn.(2) as

$$\alpha = \left[\gamma - \left(\frac{J_{2D}}{J_1^2} \right) \frac{1}{F_s} \right] \left(\frac{P_a}{J_1} \right)^{n-2} \quad (10)$$

The averaged values of a_1 and η_1 in Eqn.(5) are obtained from various tests.

The non-associative parameter, κ in Eqn.(7) is determined as follows:

The flow rule is

$$d\varepsilon_{11}^P = \lambda \frac{\partial Q}{\partial \sigma_{11}}$$

$$\text{and } d\varepsilon_v^P = 3\lambda \frac{\partial Q}{\partial J_1} \quad (11)$$

$$\text{or } \frac{d\varepsilon_v^P}{d\varepsilon_{11}^P} = \left(3 \frac{\partial Q}{\partial J_1} \right) / \left(\frac{\partial Q}{\partial \sigma_{11}} \right) \quad (12)$$

where, $d\varepsilon_{11}^P$ is axial plastic strain increment, σ_{11} is axial stress and $d\varepsilon_v^P$ is volumetric plastic strain increment. The ratio of $d\varepsilon_v^P/d\varepsilon_{11}^P$ can be obtained as the slope of the observed ε_{11}^P vs. ε_v^P response by choosing a point in the ultimate state. The value of α_Q which is represented in the right hand side of the Eqn.11 can then be found. Using this value along with α and r_v at ultimate condition, average values of are determined.

The Young's modulus, E and Poisson's ration, ν are obtained from the initial portion of the stress-strain-volume change response. The dependency of E on confining pressure is expressed using Janbu's relationship as

$$E = k P_a \left(\frac{\sigma_3}{P_a} \right)^{n^1} \quad (13)$$

where, k and n^1 are the constants obtained from observed experimental results.

Reinforced Soil

Drained triaxial tests were conducted on a natural and reinforced soil using woven geotextile (Soni, 1995; Varadarajan et al., 1999). Ennore sand procured from the coastal area near Chennai, in the southern part of Indian subcontinent was used. The physical properties were:

- specific gravity = 2.64,
- uniformity coefficient = 1.63,
- effective size $D_{10} = 0.40$ mm,
- median size $D_{50} = 0.60$ mm,
- maximum dry densities = 18 kN/m^3 , and
- minimum dry densities = 16 kN/m^3 .

The soil particles were derived from quartz and are sub-rounded and rounded in shape. For reinforcement, Geolon, a woven geotextile manufactured by Bombay Dyeing Company, India and needle punched non-woven geotextile manufactured by Shri Dinesh Mills Company were used. The characteristics of the reinforcements are shown in Table 1. A computer controlled triaxial testing system (Fig.3) acquired from M/s GDS instruments Ltd. was used for the testing. The system uses three digital pressure controllers, digital interface and axial loading system. The system is controlled by a desk-top computer and provides full test control, real time logging to disk, data reduction and

TABLE 1 : Reinforcement Properties

Properties	Non-Woven Geotextile	Woven Geotextile
Material / Colour	Polypropylene / White	Polypropylene / White
Thickness (mm)	2.8	0.64
Stiffness modulus (kN/m)	23.13	660
Yield strength (kN/m)	11.65	19.93

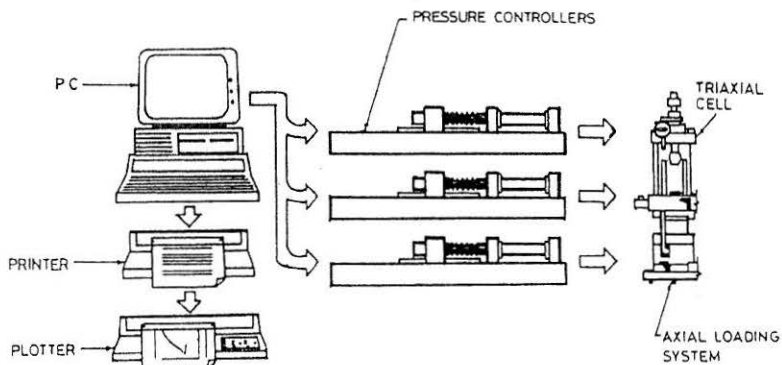


FIGURE 3 : Schematic Diagram of GDS Triaxial Testing Equipment

reports data presentation by tabulation as well as by graphics plotter. Stress and strain controlled testing under drained and undrained condition using various stress-paths are among the various features available in the test system.

The stress-paths used were:

hydrostatic compression, HC,
 conventional triaxial compression, CTC,
 triaxial compression, TC,
 reduced triaxial compression, RTC,
 conventional triaxial extension, CTE,
 triaxial extension, TE and
 reduced triaxial extension, RTE.

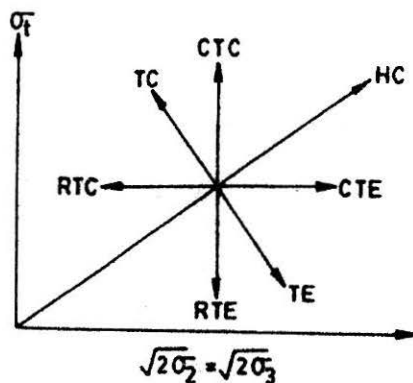


FIGURE 4 : Stress-Paths used for the Tests on Reinforced Soil

TABLE 2 : Material Parameters for Natural and Reinforced Soils

Parameter		Natural Soil	Reinforced Soil RINW*
Elastic Constants	k	600	500
	n'	0.95	0.96
	ν	0.34	0.37
Ultimate Parameters	m	-0.50	-0.50
	γ	0.071	0.072
	β	0.610	0.687
Phase change parameter	n	2.54	2.98
Hardening Parameters	a_1	0.366×10^{-3}	0.405×10^{-5}
	β_1	0.711	1.611
Non-associative parameter	κ	0.228	0.276

* RINW — Single Layer of Non-woven reinforcement

The various stress-paths used for testing the reinforced soil are shown in Fig.4.

The material parameters determined for the natural and reinforced soil are presented in Table 2. The plots of the basic function F_b and shape function F_s are shown in Figs.5 and 6 respectively for single layer, R1NW and two layer, R2NW of non-woven geotextile reinforced samples.

The prediction of stress-strain relationship has been made by integrating the incremental stress-strain relation as

$$\{d\sigma\} = [C^{ep}]\{d\varepsilon\} \quad (14)$$

where $\{d\sigma\}$ and $\{d\varepsilon\}$ are the incremental stress and strain vectors and $[C^{ep}]$ is the elastoplastic constitutive matrix.

The predictions of the stress-strain-volume change behaviour were made for two groups of tests, Group A tests used for determining material parameters and Group B tests not used for evaluating material parameters.

The predicted and observed stress-strain-volume change relationships for a few tests are shown in Figs.7 to 9. The predictions are generally satisfactory.

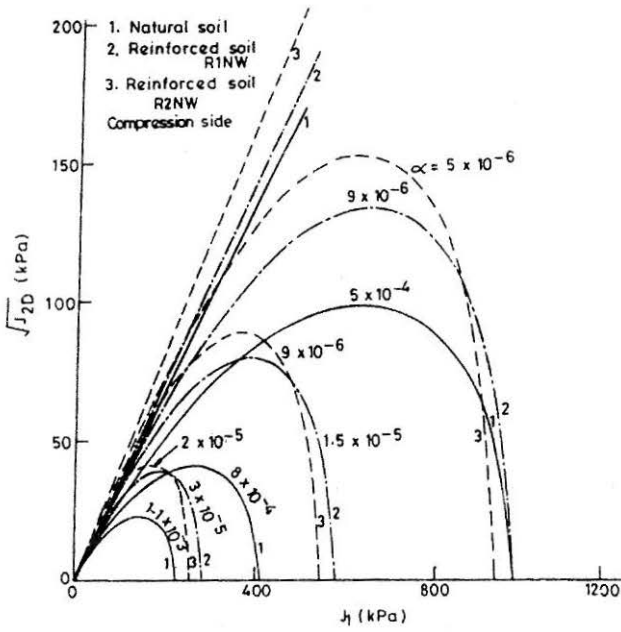


FIGURE 5 : Plot of Basic Function F_b in the $J_1 - \sqrt{J_{2D}}$ Plane for Natural Soil and Reinforced Soil R1NW and R2NW for Compression Side ($S_r = 1$)

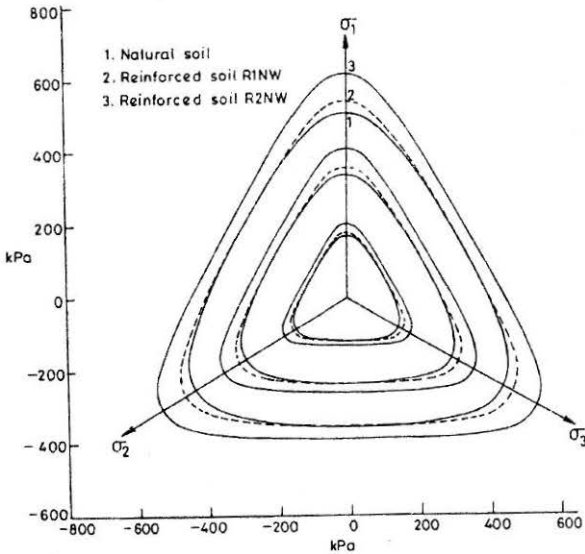


FIGURE 6 : Plot of Shape Function F_s in the Octahedral Plane for Natural Soil and Reinforced Soil, R1NW and R2NW

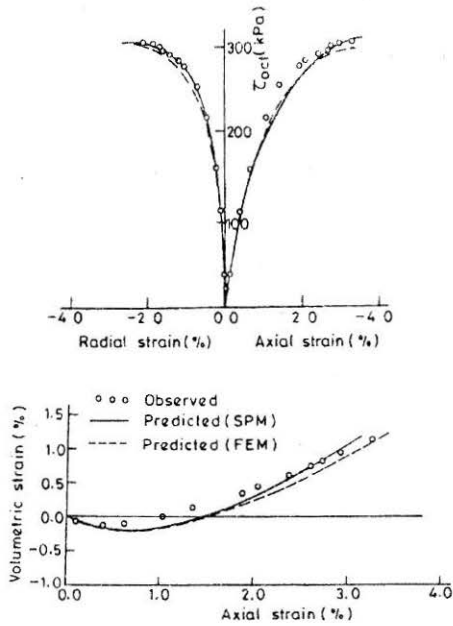


FIGURE 7 : Stress-Strain-Volume Change Response of Natural Soil for CTC Path, $\sigma_c = 200$ kPa (Group A)

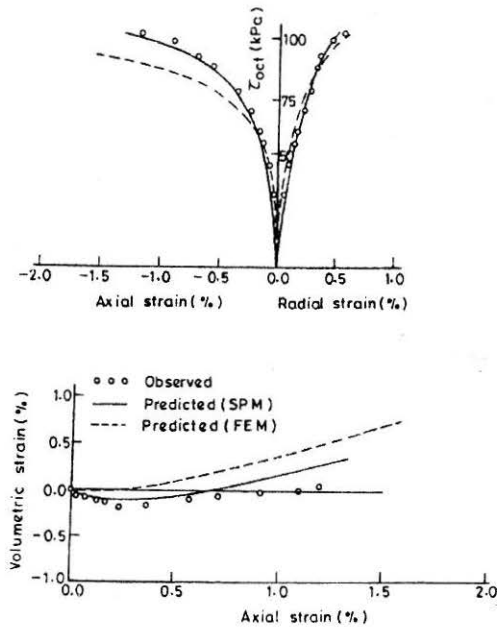


FIGURE 8 : Stress-Strain-Volume Change Response of Reinforced Soil R1NW for TE Path at $\sigma_c = 200$ kPa (Group A)

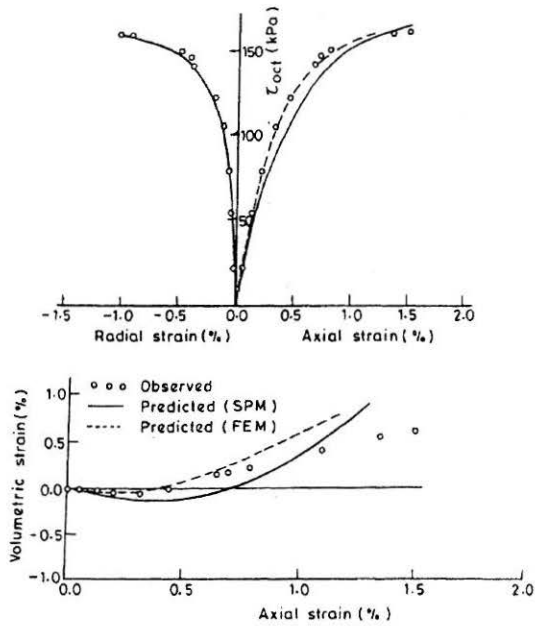


FIGURE 9 : Stress-Strain-Volume Change Response of Reinforced Soil R1NW for TC Path at $\sigma_c = 200$ kPa (Group B)

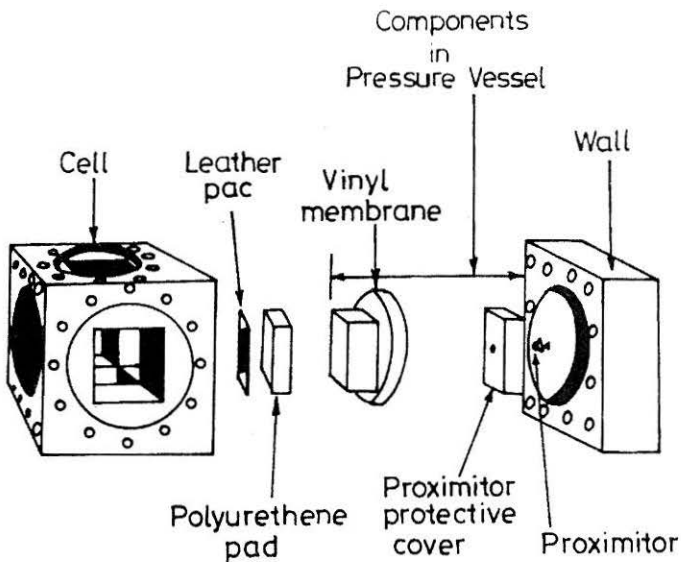


FIGURE 10 : Cubical Triaxial Cell

Rock Salt

Multiaxial tests were conducted on the cubical specimens of rock salt by truly triaxial device (Desai and Varadarajan, 1987). Rock salt, used for testing was collected from New Mexico, USA and belongs to the Salado formation. It has light pink colour and consists of essentially halite crystals with less amounts of anhydrite, poly-halite, clay and silt. Specific gravities and porosities average 2.2 and 0.6% respectively. Cubical specimens ($10 \times 10 \times 10$ cm) were cut from a block of rock salt and used for testing.

The schematic diagram of the test cell is shown in Fig.10. The loading on the three perpendicular faces in the three directions was applied by hydraulic pressure using hand pumps. The loading was applied in several increments. After each load increment, the deformation in each face of the specimen was measured using proximeter probes. A data acquisition system was used to record displacements of the specimen and the loading applied. Various stress-path tests were conducted by applying appropriate load increments on each of the three pairs of loading faces. The stress-paths used included HC, CTC, CTE and TE paths.

HISS model was used to characterize the behaviour of rock salt. In this case, F_s was expressed as

TABLE 3 : Material Constants for Rock Salt

Elasticity	K	14,989 MPa
	G	8413 MPa
	E	20,685 MPa
	ν	0.27
Cohesive / Tensile Strength		R 1.79 MPa
Plasticity: Ultimate	m	-0.50
	γ	0.0945
	β	-0.995
	β_1	0.00479
		$\beta_0 = 1.0$ MPa
	n	3.0
	a_1	0.0001785
Hardening		η_1 0.2322
		$\alpha_0 = 1.0$ MPa
Nonassociative		κ 0.275

$$F_s = \left(\exp \frac{\beta_1}{\beta} J_1 - \beta S_r \right)^m \quad (15)$$

where β and β_1 are constants ($\beta_0 = 1.0$ MPa). Change of F_s with J_1 allows for observed variation in the shape of ultimate yield surface with J_1 .

Material constants were obtained from the test results and are presented in Table 3. Figure 11 shows the comparisons between observed ultimate stresses from various tests with respect to predicted surfaces in $J_1 - \sqrt{J_{2D}}$ space for different (but similar) rock salts. Predictions and observations in octahedral and triaxial planes are shown in Fig.12. Figures 13 and 14 show comparisons between predicted and observed stress-strain and volumetric responses for CTC and TE paths using both the associative and non-associative models. The predictions, in general, are satisfactory for non-associative model.

Constitutive Model using Disturbed State Concept

Features of the Model

As a material deforms under applied loading, an initially intact material undergoes micro-structural changes, which may involve reorientation of particles, damage, microcracking and induced anisotropy (Desai, 1995, 2001). During such microstructural changes, the material may remain continuous as in the case of soft clay or become discontinuous as in the case of dense sand, rock and concrete. The latter implies damage model.

A deforming material is considered to be a mixture of continuous and discontinuous parts. The latter can involve relative motions between particles due to micro-cracking, slippage etc. For the element of the same material, the reference states are considered to be its (initial) continuous or relatively intact (RI) state and the fully adjusted (FA) state that results from the transformation of the RI state due to factors such as particle (relative) motions and micro-cracking (Fig.15). The disturbed state concept (DSC) is based on the basic physical principle that the behaviour exhibited by the interacting mechanisms of components in a mixture can be expressed in terms of the responses of the components through a coupling function which is called the disturbance function, D . This function includes the damage parameter as well.

An initially intact material without any flaws, cracks or discontinuities would transform continuously with loading, unloading and reloading (collectively referred as loading) from RI state to FA state. If the material before loading contains initial flaws, cracks or discontinuities (disturbances),

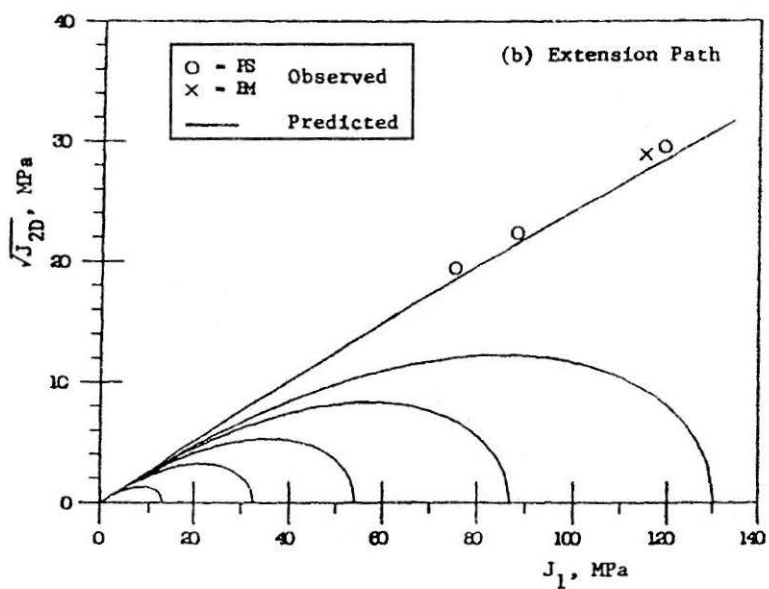
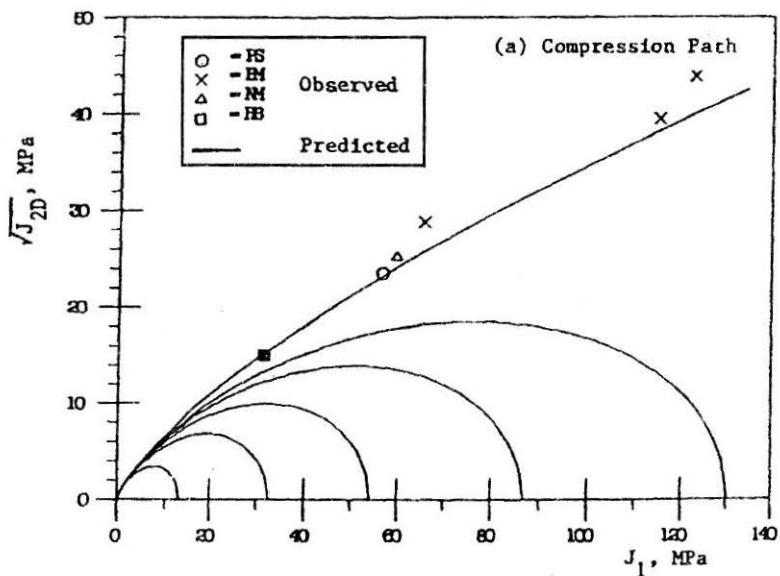


FIGURE 11 : Plot of F in $J_1 - \sqrt{J_{2D}}$ Plane for Rock Salt

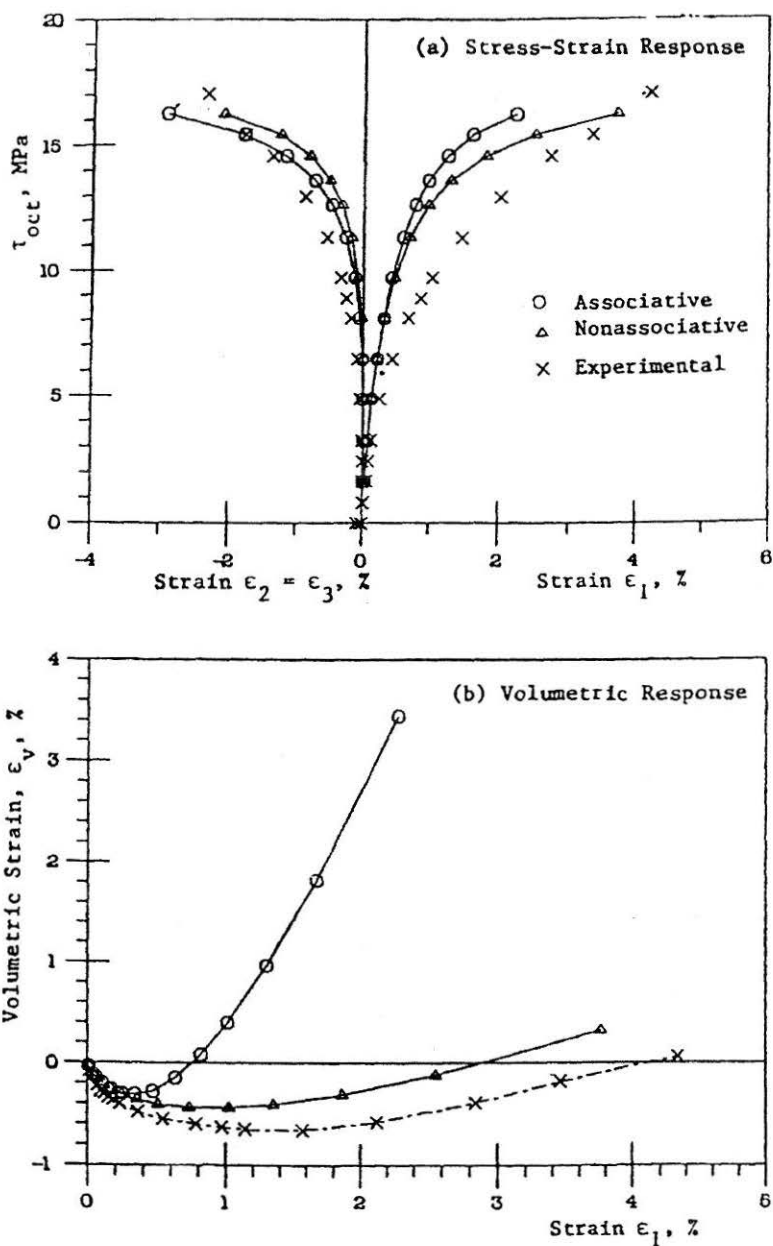


FIGURE 13 : Comparison Between Predictions and Observations for CTC Test, $\sigma_c = 3.45 \text{ MPa}$

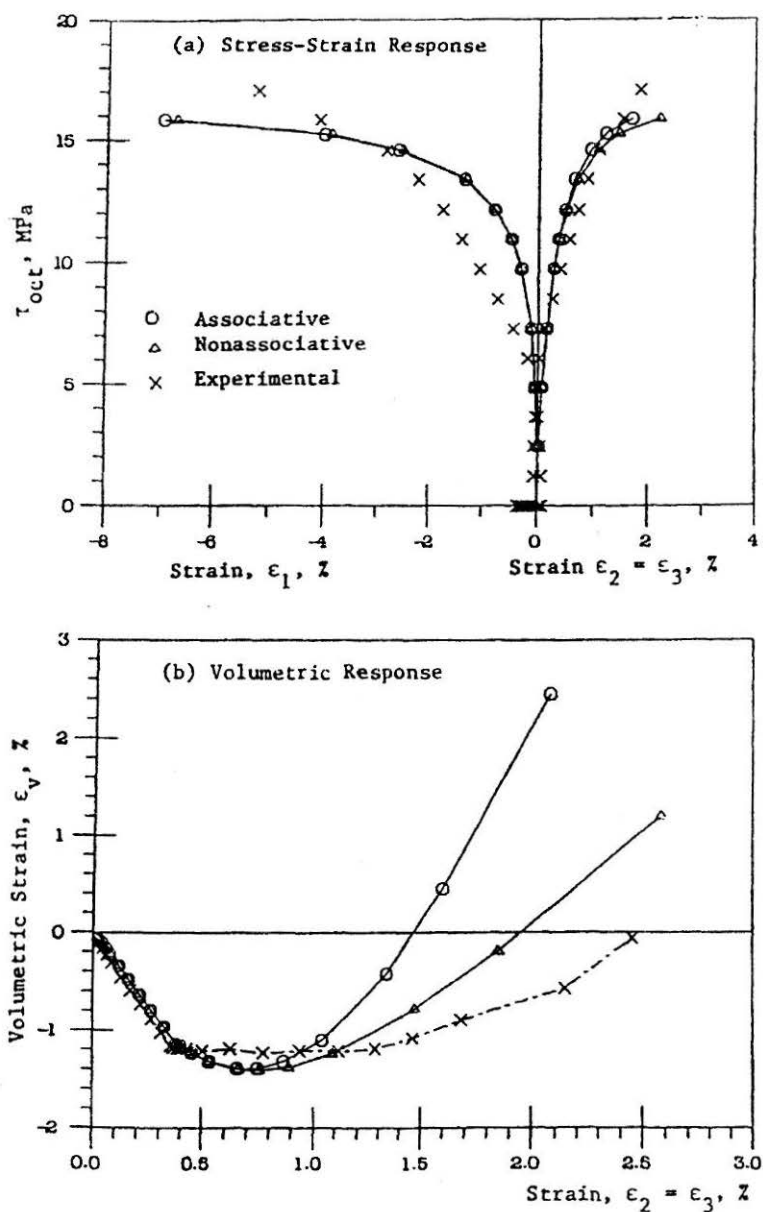
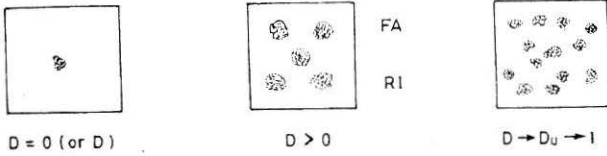
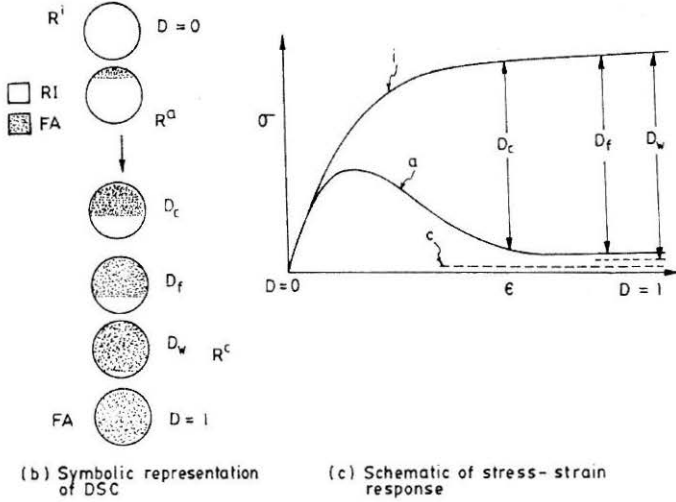


FIGURE 14 : Comparison Between Predictions and Observations for TE Test, $\sigma_c = 27.56$ MPa



(a) Clusters of RI and FA parts



(b) Symbolic representation of DSC

(c) Schematic of stress- strain response

FIGURE 15 : Representation of Disturbed State Concept (Desai, 1995)

these would influence the subsequent behaviour. The DSC can provide a unified and holistic modeling approach to characterize the entire stress-strain response of geologic materials exhibiting strain-softening behaviour. The complete details of the DSC are given in various publications (Desai, 1995; Desai, 2001). The salient features of the DSC are described herein. In the DSC, the material response is expressed in terms of the responses in the continuous (RI) and the discontinuous (FA) parts as

$$\sigma_{ij}^a = (1-D)\sigma_{ij}^i + D\sigma_{ij}^c \quad (16)$$

where a , i , and c superscripts denote observed (averaged), RI and FA states, respectively. The coupling (disturbance) function between the two states can be written in the form of

$$D = D_u \left[1 - \exp(-A \xi_D^Z) \right] \quad (17)$$

where D_u , ultimate disturbance, A and Z disturbance parameters and ξ_D is deviatoric part of plastic strain trajectory given by

$$\xi_D = \int (dE_{ij}^p dE_{ij}^p)^{1/2} \quad (18)$$

The relatively intact state is assumed as associated elastoplastic hardening response and is characterized by HISS model as

$$F = \frac{J_{2D}}{P_a^2} - \left[\alpha \left(\frac{\bar{J}_1}{P_a} \right)^n + \gamma \left(\frac{\bar{J}_1}{P_a} \right)^2 \right] (1 - \beta S_r)^m = 0 \quad (19)$$

$$\text{and } \bar{J}_1 = J_1 + 3R \quad (20)$$

where R is the bonding stress.

As a simplification, it is assumed that strains in RI and FA states are equal, that is, there is no motion between the RI and FA states. Additional assumptions have been made that the material in FA states can carry no shear stress, but can carry hydrostatic stress, which is same in the RI and FA states.

Determination of Material Parameters

The procedure for the determination of material parameters has been described in detail in various references (Desai. et. al 1986, Desai and Wathugala 1987, Desai 1995 and Desai 2001). It is briefly presented herein.

Disturbance Parameters

Rearranging Eqn.(16) and the fact that σ_{ij}^a and σ_{ij}^i lie on the same deviatoric plane, perpendicular to the hydrostatic axis, as $J_1^c = J_1^i$, yields

$$\sqrt{J_{2D}^a} = \sqrt{J_{2D}^i} (1 - D) \quad (21)$$

where a and i superscripts denote the observed (averaged) and RI states, respectively. Therefore, the D_u disturbance at ultimate stage can be obtained as

$$D_u = 1 - \frac{(\sqrt{J_{2D}})_r}{(\sqrt{J_{2D}})_u} \quad (22)$$

where r and u subscripts denote the residual and ultimate stages corresponding to the observed (averaged) and RI states, respectively. The

ultimate stage ($\sqrt{J_{2D}}$) can be found from the RI state response (1.1 to 1.15 times the peak value). Therefore, for each test, a particular value of D_v could be calculated. Based on the Eqn.(21), the value of D can be determined at each observed point of stress-strain curve, for every test. Conducting a least squares analysis on the Eqn.(17), the disturbance parameters, A and Z are determined for each experimental test. The average of the disturbance parameters for all the tests is taken as overall disturbance parameters for the material.

The trajectory of plastic strain, ξ used in the determination of various DSC parameters is expressed as

$$\xi = \int (d\epsilon_1^P \cdot d\epsilon_1^P + d\epsilon_2^P \cdot d\epsilon_2^P + d\epsilon_3^P \cdot d\epsilon_3^P)^{1/2} \quad (23)$$

The values of, ξ , ξ_v , and ξ_D (volumetric and deviatoric parts of ξ respectively) are obtained at j^{th} point of the observed stress-strain curve as

$$\xi = \sum_{i=1}^j d\xi = \sum_{i=1}^j \left[(d\epsilon_1^P)^2 + (d\epsilon_2^P)^2 + (d\epsilon_3^P)^2 \right]^{1/2} \quad (24)$$

$$\xi_v = \sum_{i=1}^j d\xi_v = \sum_{i=1}^j \frac{|d\epsilon_1^P + d\epsilon_2^P + d\epsilon_3^P|}{\sqrt{3}} \quad (25)$$

$$\xi_D = \sum_{i=1}^j d\xi_D = \sum_{i=1}^j (d\xi^2 - d\xi_v^2)^{1/2} \quad (26)$$

Ultimate Parameters

After the disturbance parameters are known, the value of D is known at all the observed points, Eqn.(16) can be rearranged to yield

$$\sigma_{ij}^i = \frac{\sigma_{ij}^a}{1-D} - \frac{D}{1-D} \cdot \left(\frac{J_1^i}{3} \right) \delta_{ij} \quad (27)$$

Thus, the stress in RI state, σ_{ij}^i , can be computed from Eqn.(27) for the observed (averaged) stress, σ_{ij}^a , values. At the ultimate stage, the value of α approaches zero: thus for the RI state, the HISS- δ_0 yield surface degenerates to an open surface intersecting J_1^i axis at infinity. Using this

condition in the yield function, i.e. Eqn.(19), the slope of the ultimate line is derived as

$$\frac{\bar{J}_1'}{\sqrt{J_{2D}'^2}} = \left(\frac{(1 - \beta S_r)^{1/2}}{\gamma} \right)^{1/2} \quad (28)$$

where $S_r = 1$ for compression and $S_r = -1$ for extension tests. The ultimate parameters are found by conducting least squares analysis on Eqn.(28) i.e. $(J_1, \sqrt{J_{2D}})$ on the points corresponding to the ultimate stresses for the (at least two triaxial) tests in $(J_1, \sqrt{J_{2D}})$ plane. The ultimate parameters γ and β can be determined as follows

$$p_1 = \tan \theta_c = \left[\sqrt{\gamma} (1 - \beta)^{m/2} \right]_c = \frac{2}{\sqrt{3}} \left(\frac{\sin \phi_c}{3 - \sin \phi_c} \right) \quad (29)$$

$$p_2 = \tan \theta_E = \left[\sqrt{\gamma} (1 + \beta)^{m/2} \right]_E = \frac{2}{\sqrt{3}} \left(\frac{\sin \phi_E}{3 + \sin \phi_E} \right) \quad (30)$$

$$\beta = \frac{1 - p^{2/m}}{1 + p^{2/m}} \quad (31)$$

where
$$p = \frac{\tan \theta_c}{\tan \theta_E} \quad (32)$$

The value of γ is found from either Eqn.29 or 30.

In the present analysis, in the absence of the observed results from other stress paths, the friction angle in compression and extension sides of the yield surface is assumed to be same, i.e. $\phi_c = \phi_E$.

Bonding Stress

The value of bonding stress, R, is determined by extending the ultimate line. The intersection of ultimate line with J_1' axis yields the value equal to three times of R on the negative side.

Phase Change Parameter

The phase change parameter, n , is calculated using the zero plastic

volume change condition, $\partial F / \partial J_1 = 0$. Based on Eqn.(19), this leads to the expression for n as

$$n = \frac{2}{1 - \left(\frac{J_{2D}}{J_1^2} \right) \cdot \frac{1}{F_s \gamma}} \Bigg|_{d\varepsilon_p^p=0} \quad (33)$$

The value of n is calculated using the equation for each test. An average of n values for different tests is taken as an overall value of n for the material.

Hardening Parameters

The hardening function α is assumed as the function of a single parameter ξ as

$$\alpha = \frac{a_1}{\xi^{\eta_1}} \quad (34)$$

where a_1 and η_1 are the material parameters; and ξ is the trajectory of plastic strains as

$$\xi = \int (d\varepsilon_{ij}^p d\varepsilon_{ij}^p)^{1/2} \quad (35)$$

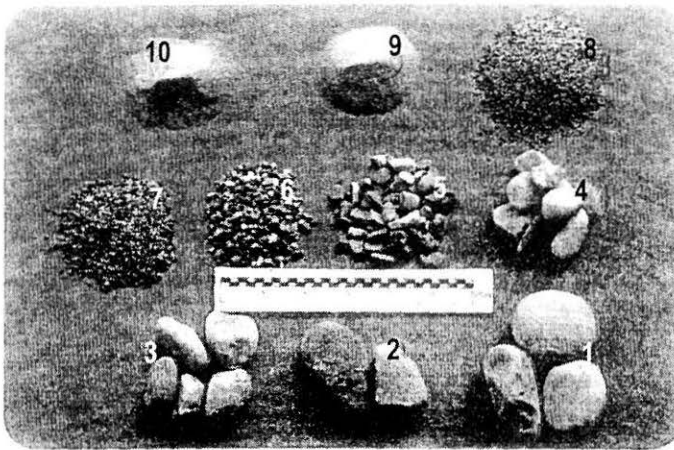
For each test, at all the observed points of the stress-strain curve, the value of ξ is known. The value of the hardening function for the observed points is calculated using the yield function, i.e. Eqn.(19). Substituting the values of α and ξ in Eqn.(34) and conducting least squares analysis, the hardening parameters, a_1 and η_1 are obtained for each test. The average value of a_1 and η_1 found from various tests are taken as overall values of the hardening parameters a_1 and η_1 .

Elastic Parameters

The two elastic constants for an isotropic material, Young's modulus, E , and Poisson's ration, ν , are determined from the average slopes of the unloading-reloading curves. Thus, the slope of the deviator stress ($\sigma_1 - \sigma_3$) vs. major principal strain, ε_1 , curve yields the value of E and from the minor and major principal strains the Poisson's ration, ν is determined.

Rock-fill Material

The rock-fill material obtained from Ranjit Sagar Hydropower Project



No.	1	2	3	4	5
Particle Size (mm)	80 - 60	60 - 50	50 - 40	40 - 25	25 - 10
No.	6	7	8	9	10
Particle Size (mm)	10 - 4.75	4.75 - 2.0	2.0 - 0.425	0.425 - 0.075	< 0.075

FIGURE 16 : Ranjit Sagar Rock-Fill Material

located in Gurdaspur district of Punjab state was used. The rock-fill material was a transported riverbed material consisting of rounded/sub-rounded particles (Fig.16). The material was derived from Upper Shivalik rock of sedimentary origin. It contains pieces of conglomerate, sandstone, quartzite/shale, clay-stone, grits of chart and jasper, other material of older rocks and recent alluvium. The gradation curve of the rock-fill material is shown in Fig.17. Three modeled gradation curves were derived using parallel gradation modeling technique (Lowe, 1964) having a maximum particle size of 80, 50 and 25 mm respectively as shown in Fig.17.

Consolidated drained triaxial tests were conducted on the modeled rock-fill materials with various confining pressures. Large size triaxial testing facility at the Central Soil and Material Research Station, New Delhi was used. Two specimen sizes viz., 381 mm dia., 813 mm long and 500 mm dia., 600 mm long were used for testing. The details of the two triaxial cells used for the two sized of the specimens are shown in Figs. 18 and 19.

To maintain and control the applied confining pressure, an air-water pressure system with a capacity of 3 MPa was used. Axial loading was

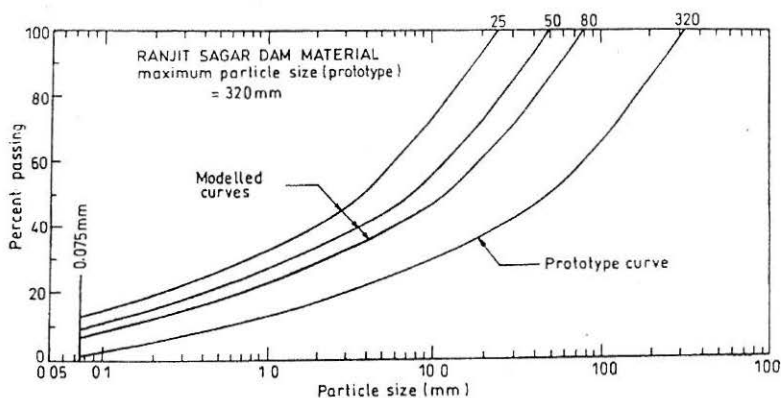


FIGURE 17 : Grain Size Distribution for Prototype and Modeled Rock-Fill Material from Ranjit Sagar Dam Site

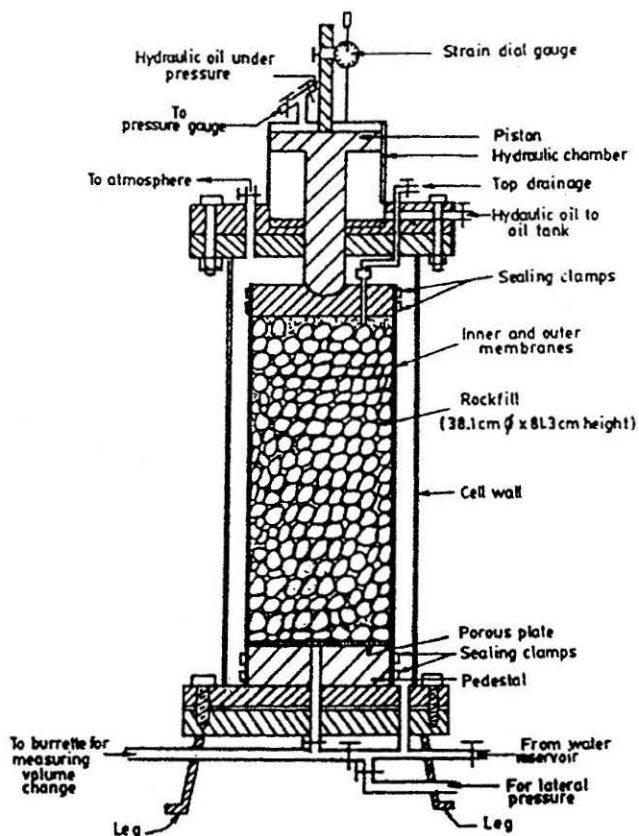


FIGURE 18 : Triaxial Cell for 381 mm Diameter and 813 mm High Specimen

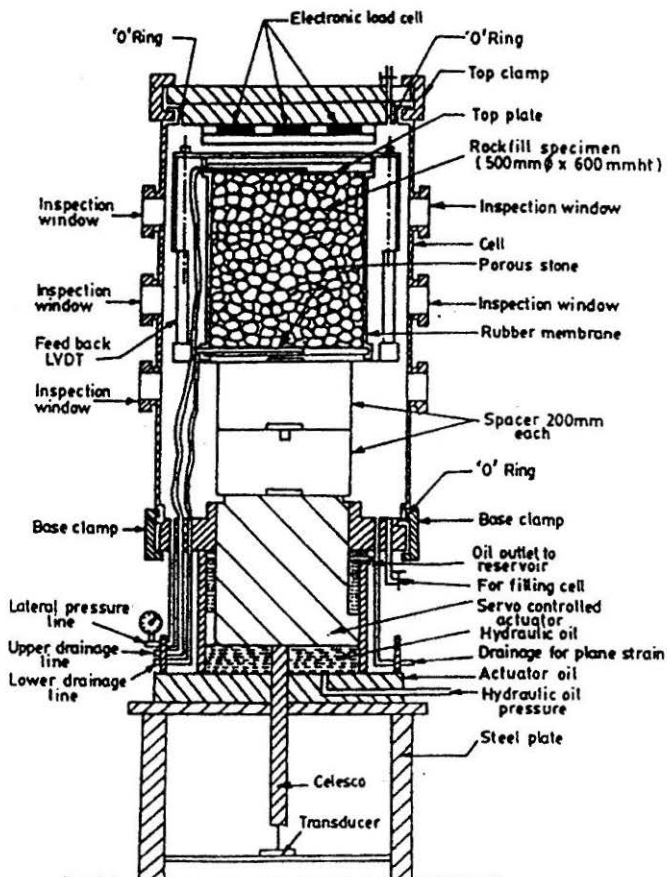


FIGURE 19 : Triaxial Cell for 500 mm Diameter and 600 mm High Specimen

TABLE 4 : Details of Drained Triaxial Tests Conducted

S.No.	Details	Ranjit Sagar Dam
1.	Maximum particle size, D_{max} (mm)	25, 50, 80
2.	Average particle size, D_{50} (mm)	3.8, 7.6, 12.0
3.	Confining pressure, (kPa)	350, 700, 1100, 1400
4.	Specimen size :	
	(a) length of the specimen (mm)	813, 600
	(b) diameter of the specimen (mm)	381, 500

TABLE 5 : Modelled Rock-fill Material Parameters

Material Constants		Ranjit Sagar Dam Material			
		Dmax (mm)			
		25	50	80	320
Elasticity	k	193.69	220.34	253.63	343.35
	n'	0.6386	0.6683	0.7146	0.8141
		0.31	0.30	0.29	0.30
Ultimate	ν	0.078	0.084	0.0912	0.1083
		0.73	0.732	0.743	0.73
Phase change	n	3	3	3	3
Hardening	α_1	0.65E-4	0.3E-4	0.985E-5	1E-6
	η_1	0.46	0.5600	0.7618	1.2865
Non-associative	κ	0.23	0.23	0.22	0.23
Disturbance	A	0.016	0.032	0.05	0.1961
	B	6.0	7.34	8.84	3.800
ϕ (degree)		31.5	33.2	35.4	40.311

applied using a hydraulic pressure unit with a capacity of 875.7 kN in the case of specimen size 381 × 813 mm. In the case of specimen size 500 × 600 mm an actuator system with a capacity of 11.5 MPa was used for axial loading. Axial strains were measured using dial gauge/LVDT and volumetric strains were measured using burette/transducer. The details of the tests are given in Table 4. The complete details of testing are given by Gupta (2000) and Varadarajan et al. (2001). The material parameters for the modeled rock-fill material were obtained from the experimental results (Gupta, 2000) and are presented in Table 5. The material parameters were extrapolated for the prototype rock-fill material based in the parameters for the modeled rock-fill material and are also presented in Table 5. These parameters may be used for the analysis of the rock-fill dam.

The prediction of stress-strain relationship was made by integrating the stress-strain relationship as

$$\{d\sigma\} = [C^{DSC}]\{d\epsilon\} \quad (36)$$

where $\{d\sigma\}$ and $\{d\epsilon\}$ are the incremental stress and strain vectors and

$[C^{DSC}]$ is the constitutive matrix for the DSC approach.

The predictions of the stress-strain-volume change behaviour were made for Group A and Group B tests. Figures 20 to 23 show the predicted and observed results for a few tests from Group A and B. It is found that the predictions are satisfactory.

Rock

Schistose rock samples were obtained from Nathpa-Jhakri Hydropower Project constructed in the middle reaches of the river Satluj in the Himachal Pradesh State. Tests were conducted on quartz mica schist, one of the rock types predominantly found at the project site. Quartz mica schist is coarse grained with well defined schistose texture and light to medium greyish white in colour (Fig.24).

Samples of 5.475 cm diameter were prepared with length/diameter ratio equal to 2 from the rock core pieces collected from the project site. The physical properties of quartz mica schist are:

specific gravity = 2.74,
dry density = 26.0 to 27.6 kN/m³ and
tensile strength = 8 MPa.

Triaxial tests were conducted on the rock samples. In order to capture the post-peak strain softening behaviour, a loading frame together with an MTS servo-controlled loading system was fabricated as shown in Fig.25. The MTS servo-controlled actuator used for loading utilized a feed back control system in which it was possible to control an experimental variable such as stress and strain automatically, continuously and precisely. A high-pressure triaxial cell with a balanced ram having a maximum cell pressure capacity of 140 MPa shown in Fig.26 was used for testing (Hashemi, 2001; Varadarajan et al., 2001). A hydraulic pressure unit that includes an oil pump with an attached high-pressure controller mechanism was used to maintain applied pressure to the sample in the triaxial cell. Fold type electrical resistance strain gauges were pasted on the mid-height of the specimens to measure axial and lateral strains on the sample. A data acquisition system, which included a computer was developed to record the axial and lateral strains and also the load on the sample applied by the servo-controlled system. The data can be acquired at a maximum rate of 60 kHz within 20 μ sec.

A series of strain-controlled triaxial compression tests were conducted on the oven dried rock specimens. Conventional triaxial compression path was used for testing. Two strain rates, a fast rate (0.1 to 0.5 mm/min) upto 50% of the peak load and a slow rate (0.0333 to 0.1 mm/min) thereafter

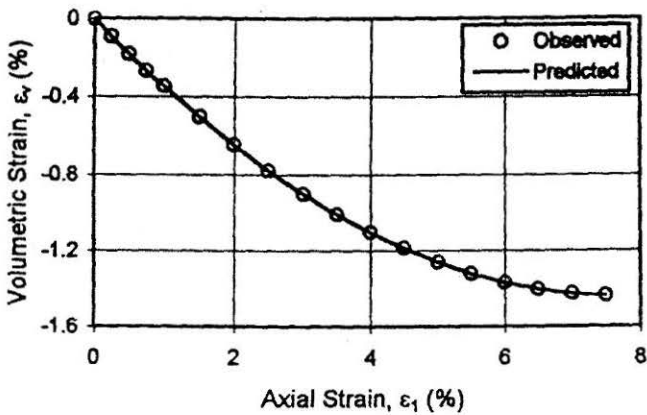
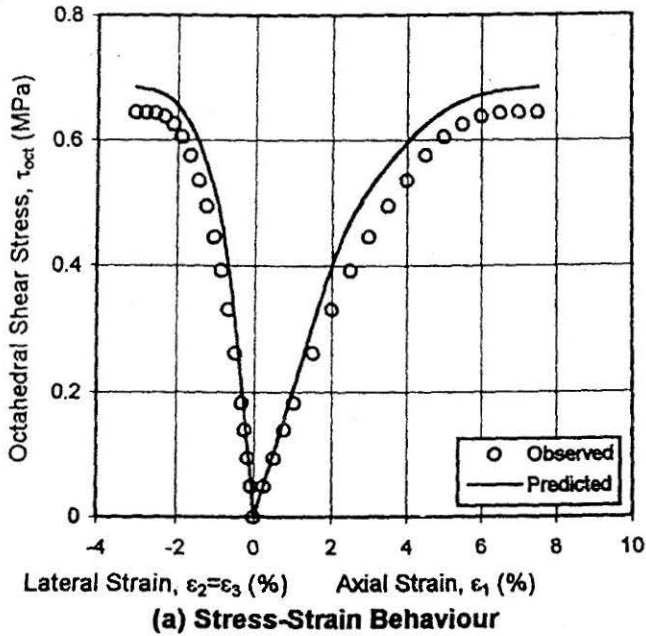


FIGURE 20 : Stress-Strain-Volume Change Response of Ranjit Sagar Rock-Fill Material ($\sigma_c = 0.35$ MPa, $D_{max} = 25$ mm)
Group A Prediction

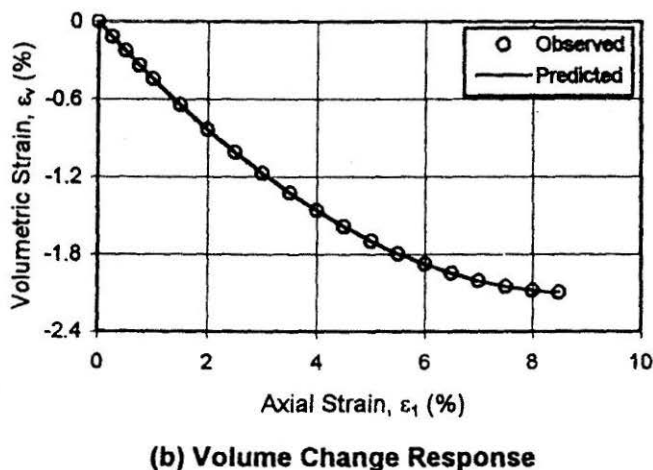
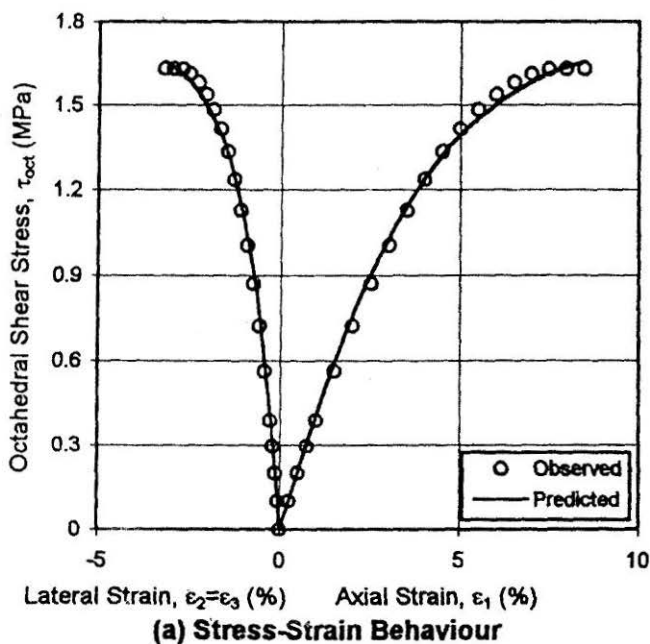


FIGURE 21 : Stress-Strain-Volume Change Response of Ranjit Sagar Rock-Fill Material ($\sigma_c = 1.1$ MPa, $D_{max} = 25$ mm)
Group B Prediction

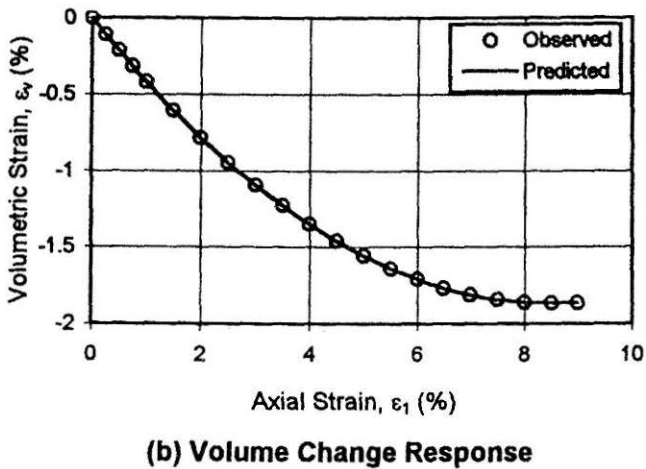
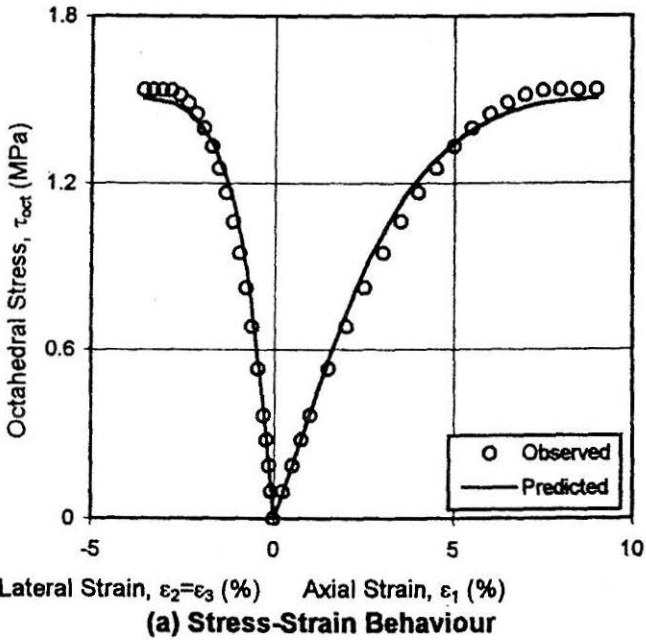
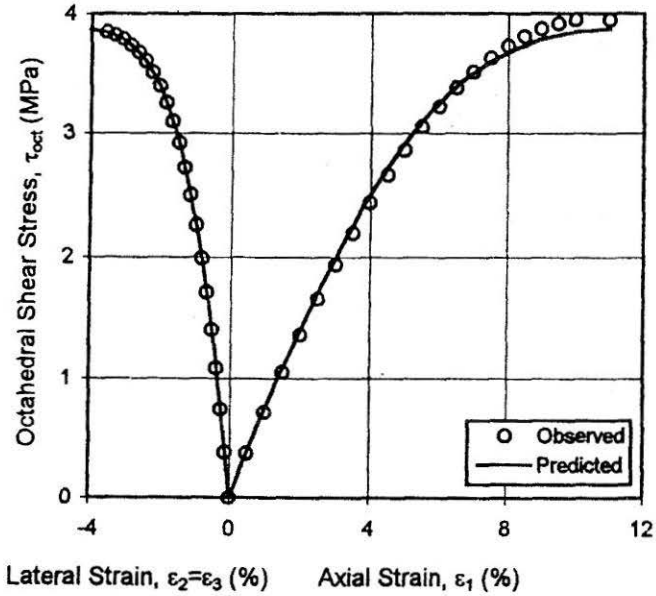
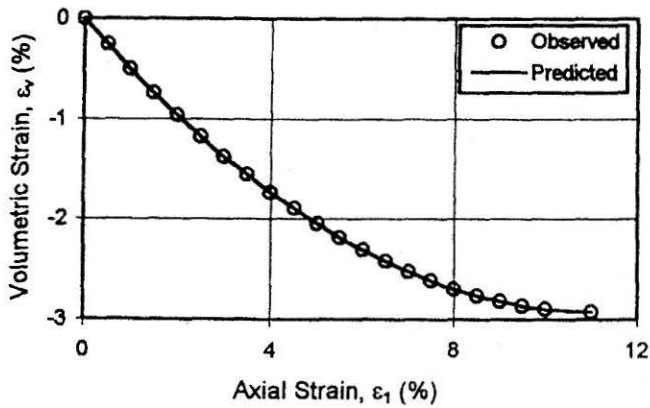


FIGURE 22 : Stress-Strain-Volume Change Response of Ranjit Sagar
Rock-Fill Material ($\sigma_c = 0.70 \text{ MPa}$, $D_{max} = 50 \text{ mm}$)
Group A Prediction



(a) Stress-Strain Behaviour



(b) Volume Change Response

FIGURE 23 : Stress-Strain-Volume Change Response of Ranjit Sagar Rock-Fill Material ($\sigma_c = 1.40$ MPa $D_{max} = 80$ mm) Group A Prediction

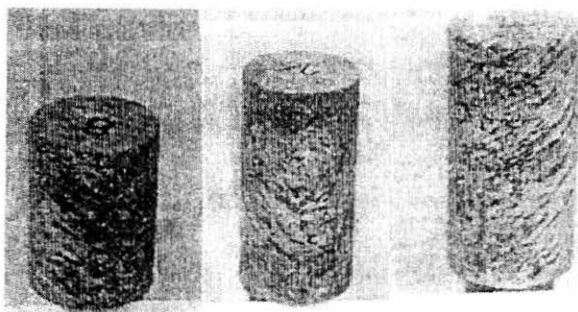
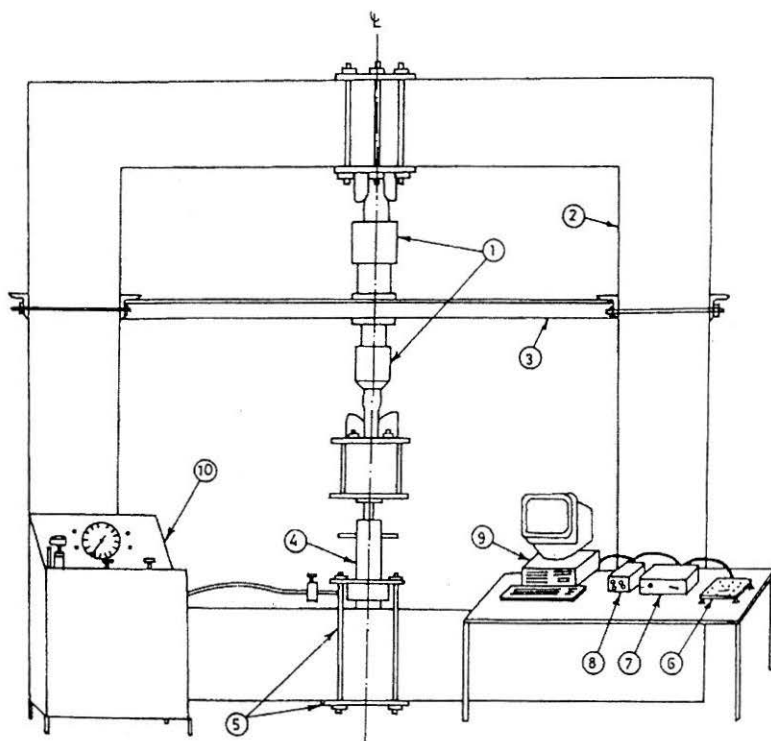


FIGURE 24 : Quartz Mica Schist Sample



EXPERIMENTAL SETUP : (1) MTS Servo-controlled Actuator, (2) Main Loading Frame, (3) Lateral Bracing of the Actuator, (4) Triaxial Cell, (5) Bracing of the Triaxial Cell, (6) Amplifier Card, (7) Relay Box, (8) Power Supply, (9) Computer Interface (including A/D Card), (10) Hydraulic Pressure Unit

FIGURE 25 : Test Setup with MTS Servo Controlled Activator

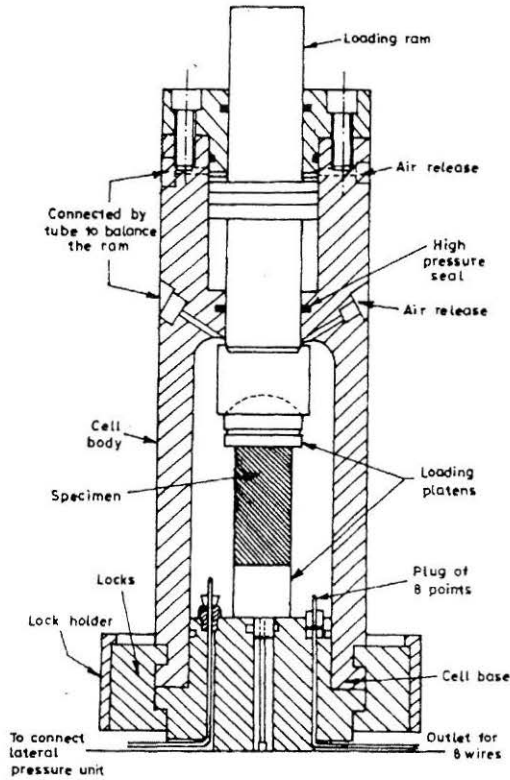


FIGURE 26 : High Pressure Triaxial Cell

were adopted in order to capture the softening behaviour. The rock samples were tested under various confining pressures (0 to 45 MPa). The material parameters for the rock samples were determined from the experimental results and are given in Table 6.

The plots in the $\bar{J}_1 - \sqrt{J_{2D}}$ space are presented along with the observed peak points of the tests for various values of hardening function α are shown in Fig.27. The plots of the yield surface in the octahedral plane are also shown in Fig.28. The predicted and observed stress-strain-volume change response of quartz mica schist for the confining pressures 22 MPa and 45 MPa are shown in Figs.29 and 30. The predictions are generally satisfactory.

Finite Element Analysis

Finite Element Method (FEM) is the mostly used numerical method in geotechnical engineering. FEM is extensively used in the Geotechnical engineering due its versatility to allow for such factors as nonhomogeneity,

TABLE 6 : Material Parameters for Intact Rock
(Quartz Mica Schist)

Parameter		Intact Rock
Elasticity	ν	0.2
	E	8591
Ultimate	γ	0.02020
	β	0.4678
Phase Change	n	5.0
Hardening	a_1	0.013E-12
	η_1	0.6
Bonding Stress (MPa)	3R	46.99
Disturbance	D_u	0.97
	A	220.71
	Z	1.339

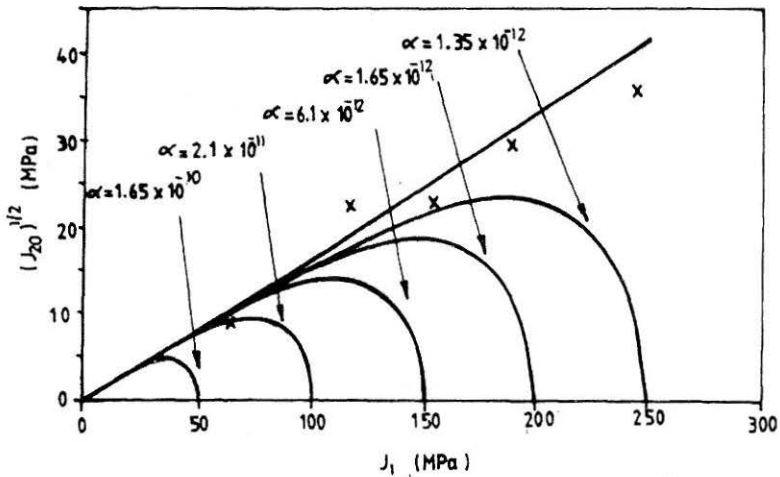


FIGURE 27 : Plot of Basic Function in the $J_1 - \sqrt{J_{2D}}$ Plane for
Quartz Mica Schist

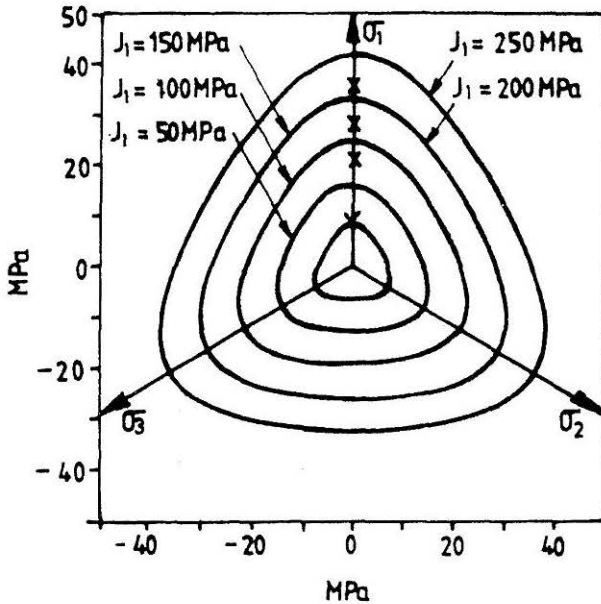


FIGURE 28 : Plot of Shape Function in the Octahedral Plane for Quartz Mica Schist

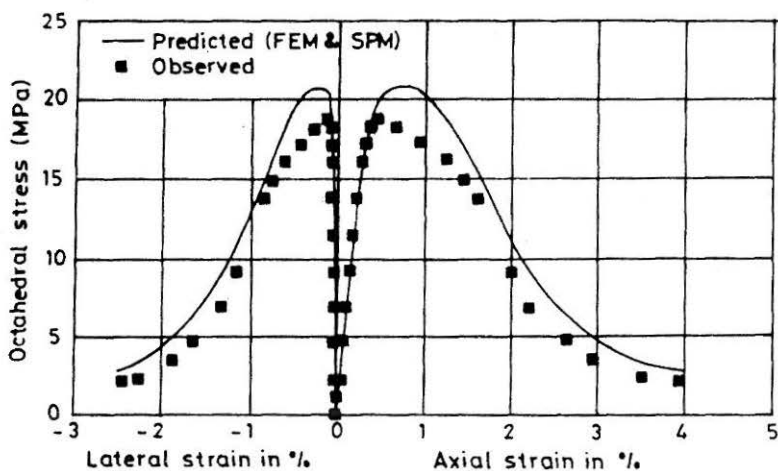
nonlinearity and anisotropic material behaviour, complex loading conditions and complicated boundary conditions.

Herein are presented the following analyses using FEM:

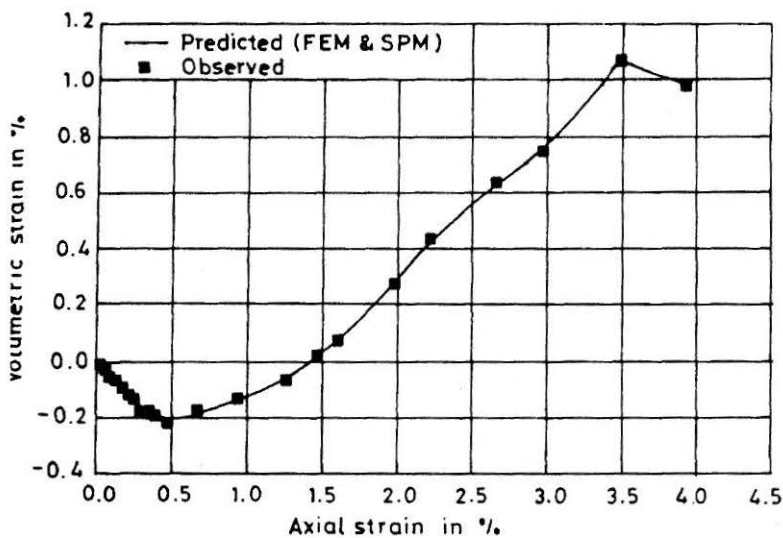
- (i) soil-structure interaction related to lateral earth pressure using hyperbolic model
- (ii) soil-structure interaction related to footing using stress-path dependent behaviour,
- (iii) stability of dam foundation using hyperbolic model,
- (iv) reinforced soil foundation using elasto-plastic model, and
- (v) powerhouse cavern using an elasto-plastic model based on disturbed state concept.

Lateral Earth Pressure

The effects of base friction and mode of wall movement on active and passive earth pressure were studied using non-linear finite element analysis by representing the stress-strain behaviour of a clayey soil using hyperbolic model (Varadarajan, 1973; Yudhbir and Varadarajan, 1974). Relevant stress-path tests were used in conducting drained triaxial tests for determining the material parameters for the model. For the analysis of active earth pressure

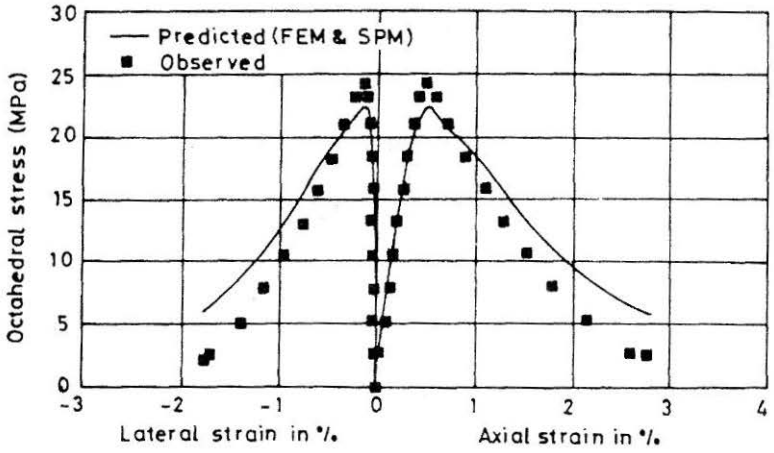


(a) Stress-Strain Behaviour

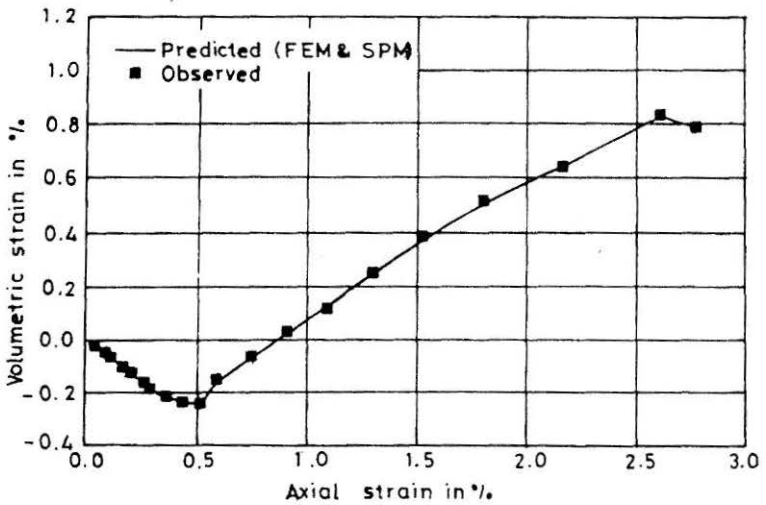


(b) Volume Change Response

FIGURE 29 : Predicted Stress-Strain-Volume Change Response for Quartz Mica Schist, ($\sigma_3 = 22$ MPa) (Group A)



(a) Stress-Strain Behaviour



(b) Volume Change Response

FIGURE 30 : Predicted Stress-Strain-Volume Change Response for Quartz Mica Schist, ($\sigma_3 = 30$ MPa) (Group B)

problem the RTC path (σ_1 constant and σ_3 decreasing) and for passive earth pressure problem, the CTC path (σ_3 constant and σ_1 increasing) were used.

Figures 31 and 32 present the effect of base friction on active and passive pressure due to lateral translation of wall. The smooth interface between the backfill soil and the rigid base gives linear earth pressure distribution similar to that given by Rankine's theory. The failure develops uniformly throughout the soil. In the case of rough base, the pressure distribution is nonlinear and for the active case the results are similar to the Taylor's model tests (Taylor 1948). In this case, the failure is reached at the bottom of the wall first and then progresses upwards. A thin failure zone develops from the toe of the wall and it has inclination of $(45 + \phi/2)$ to the horizontal in the active case and $(45 - \phi/2)$ to the horizontal in the passive case.

Lateral earth pressure distributions on the wall for rotation about the bottom and the top are shown for active and passive cases in Figs.33 and 34, respectively. It may be noted that the pressure distribution is highly nonlinear in all the cases. In the case of rotation about bottom, the pressure distributions for passive and active cases are similar to those obtained from model test on sand (Roscoe, 1970). In the case of rotation about the top, the

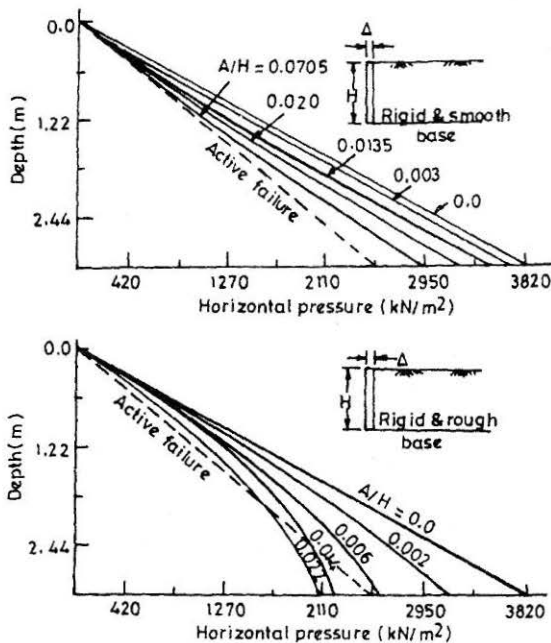


FIGURE 31 : Active Earth Pressure on Wall (Translation of Wall)

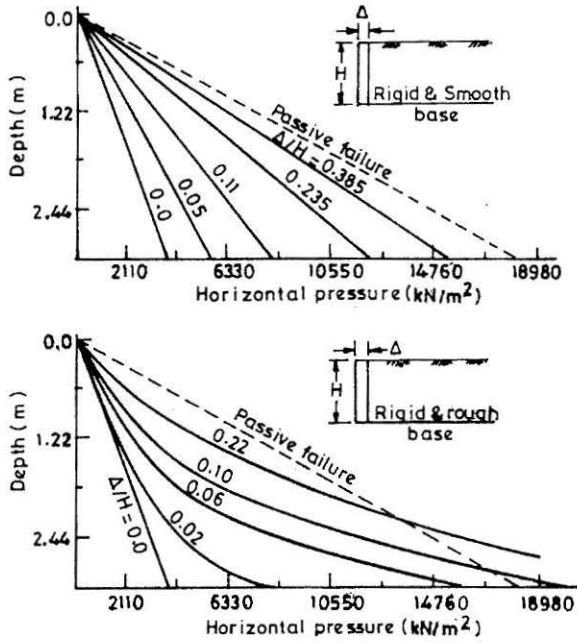


FIGURE 32 : Passive Earth Pressure on Wall (Translation of Wall)

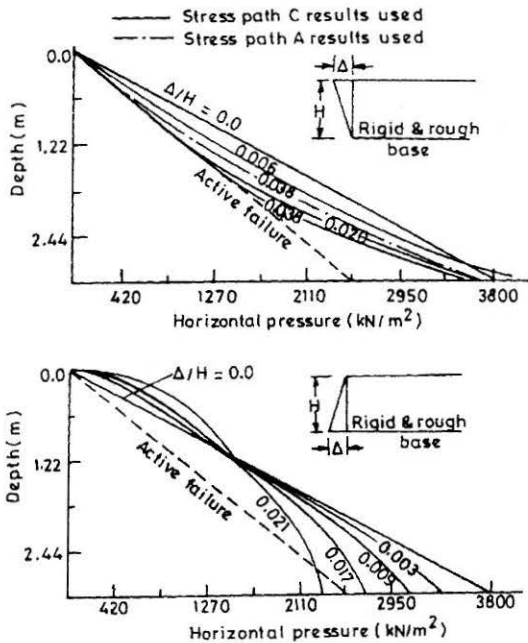


FIGURE 33 : Active Earth Pressure on Wall (Rotation of Wall)

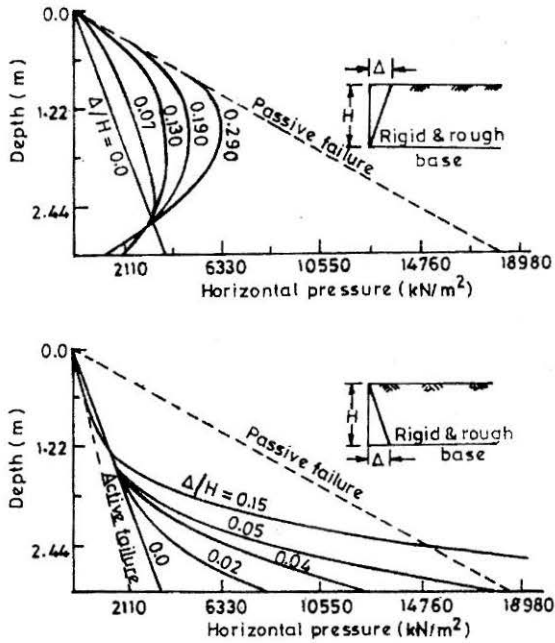


FIGURE 34 : Passive Earth Pressure on Wall (Rotation of Wall)

pressure distributions for active and passive conditions are somewhat similar to the corresponding ones for translation with the rough base. These pressure distributions are similar to those indicated by Terzaghi and Peck (1968).

Contact Pressure

The effect of stiffness of the circular footing–soil system on the contact pressure distribution was investigated by conducting stress-path dependent non-linear analysis using finite element method, (Arora, 1980, Varadarajan and Arora, 1979, 1982). The relative stiffness of the circular-footing system is defined as (Borowicka, 1936),

$$K = \frac{1}{6} \left(\frac{1 - \nu_s^2}{1 - \nu_p^2} \right) \frac{E_p}{E_s} \left(\frac{t}{a} \right)^3 \quad (37)$$

where

t = thickness of footing

a = radius of footing

E_s, ν_s = Young's modulus and Poisson's ratio of soil

E_p, ν_p = Young's modulus and Poisson's ratio of footing

The value of t , E_p and ν_p were changed to obtain the K value of 0.35, 1.84, 10.37 and 35 respectively. An equivalent constant value of E_s was taken for the soil for the calculation of K value.

The foundation medium consisted of Yamuna riverbed sand. Drained triaxial tests were conducted using various stress-paths. The samples were anisotropically consolidated along a stress-ratio line with $K_0 = 0.42$ and sheared following six different stress-paths as shown in Fig.35. Using these test results, stress-path dependent nonlinear analyses were conducted using FEM (Arora, 1980; Varadarajan and Arora, 1982).

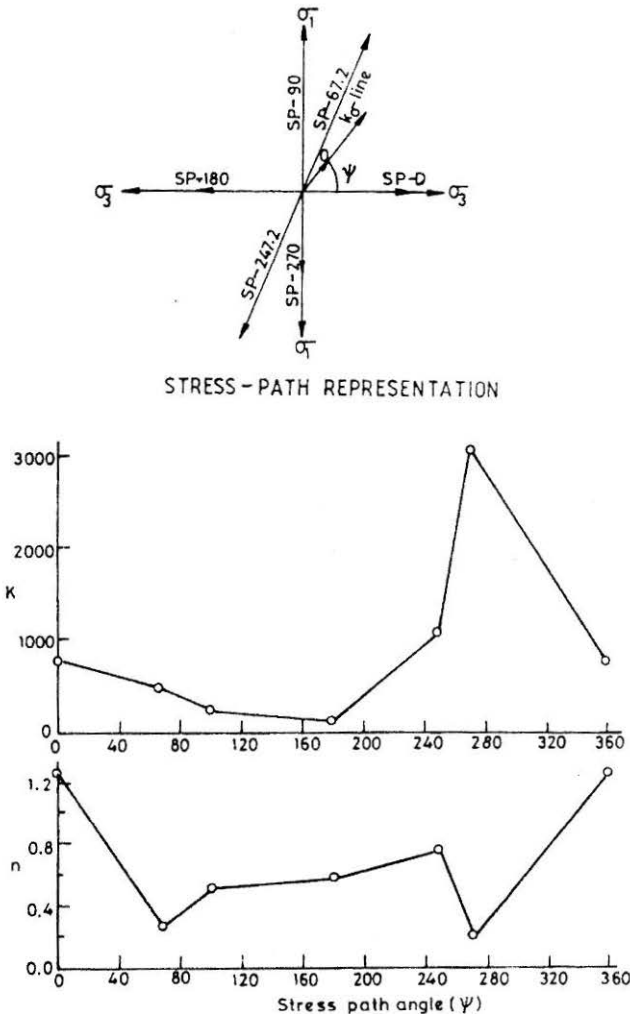


FIGURE 35 : Stress-Path Modulus Parameters K and n Relationship

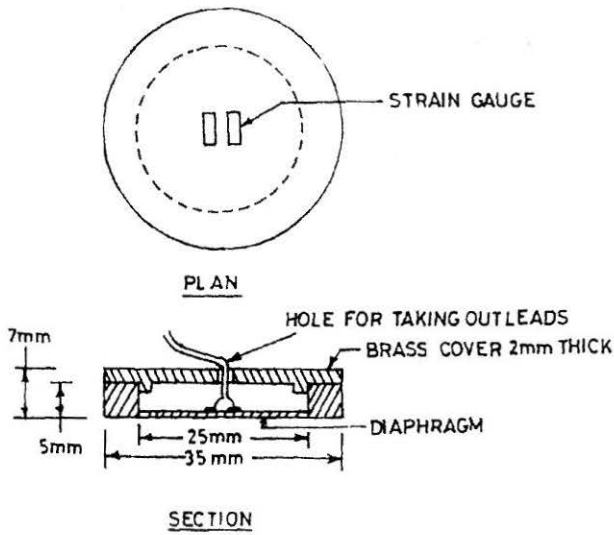


FIGURE 36 : Details of Earth Pressure Cell

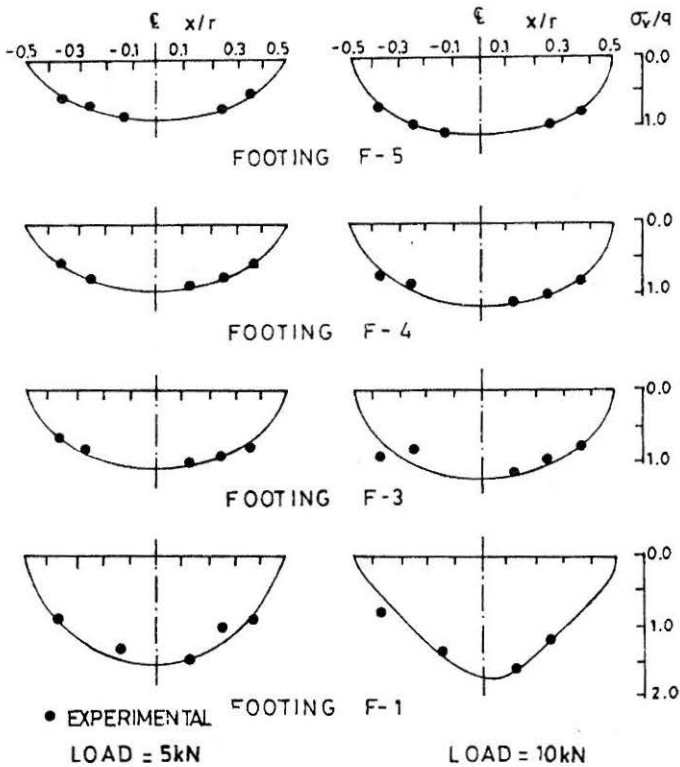


FIGURE 37 : Contact Pressure Distribution at Load 5 kN and 10 kN

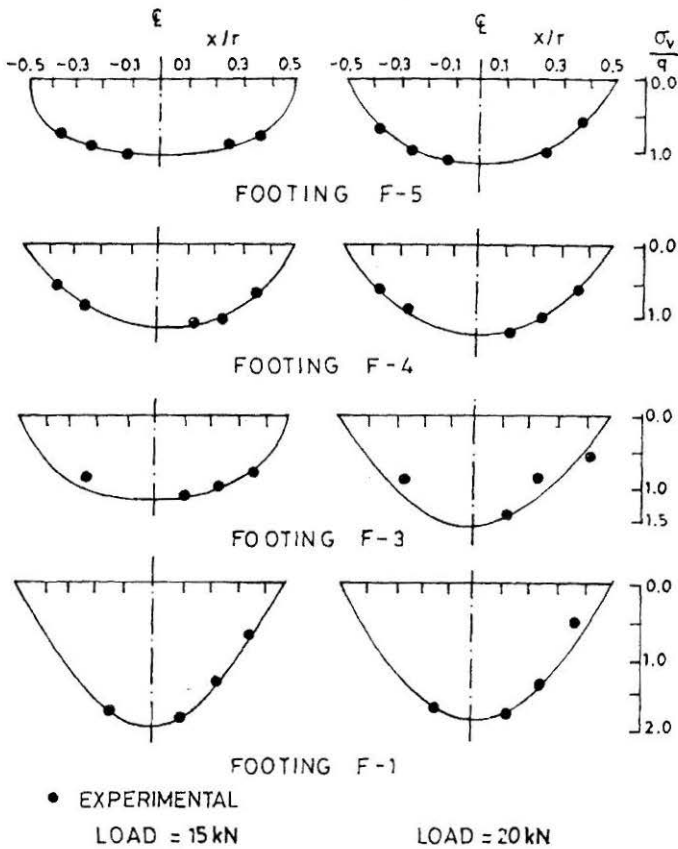


FIGURE 38 : Contact Pressure Distribution at Load 15 kN and 20 kN

The contact pressure distribution was obtained for the four stiffnesses of the footing-soil system at various loading levels. In this method, the load was applied in increments. The stress-path in each element was calculated. The modulus values corresponding to the stress-path were calculated from stress-path modulus relationship and used in the analysis.

The contact pressures predicted were compared with the experimental results. The experiments were conducted on 50 cm dia. circular footings made up of aluminium, mild steel and reinforced concrete of various thicknesses to vary the stiffness of the footing-soil system. The tests were conducted using Yamuna sand foundation. The contact pressures at the interface were measured using diaphragm type stainless steel pressure cells (Fig.36). The complete details of the tests are given in Arora (1980) and Arora and Varadarajan (1984).

The contact pressure distributions at various loads for various stiffnesses are given in Figs.37 and 38. The contact pressure distributions are parabolic. As the stiffness of the footing increases the contact pressure distribution becomes more uniform. As the load increases, the contact pressure increases at the center for all footings. The increase is more for the flexible footings. The measured contact pressures are also shown in the figure. The predicted values of the contact pressure agree with the observed values of the contact pressure.

Dam Foundation with Shear Seam

Karjan dam, which has been constructed across the river Karjan, a major tributary of Narmada river in Gujarat State, has a height of 93 m and a storage capacity of 630 million cubic meters for irrigation. The foundation of the dam consists of sound basalt. A concrete dam section in the spillway portion is shown in Fig.39. At this section, the foundation contains a thin weathered seam at a depth of 11.9 m below the foundation level. The seam is inclined towards downstream side at an angle of $3^{\circ}48'$. Concrete keys have been proposed to be constructed in the shear seam towards the downstream side (Fig.39) in order to arrest the movement along the seam thereby improving the stability of the dam foundation against sliding.

The dam foundation was investigated using FEM with and without concrete key under self-weight of the dam and reservoir full loading condition (Varadarajan and Sharma, 1989). Concrete and basalt rock were assumed to exhibit linear elastic behaviour. The shear seam was characterized by nonlinear elastic behaviour using hyperbolic model. The dam and foundation were discretised using four-noded solid elements whereas the shear seam was represented by the four-noded joint elements. Incremental method together with tangent modulus was used (Desai and Abel, 1972).

The relative horizontal displacements along the seam for the two conditions are shown in Fig.39. For the loading with the dam weight only, the movement in the seam is away from the dam section. For the case of the dam with full reservoir loading, the movement is towards the downstream direction throughout the seam, the maximum movement being near the toe of the dam. The concrete key reduces the movement in the seam significantly. The variation of the local factor of safety along the seam also shown in the figure indicates the improvement of the factor of safety due to concrete key. Figure 40 shows the contours of horizontal and vertical displacements as influenced by the concrete key. It may be noted that the effect is more pronounced in the horizontal displacements than in the vertical displacements.

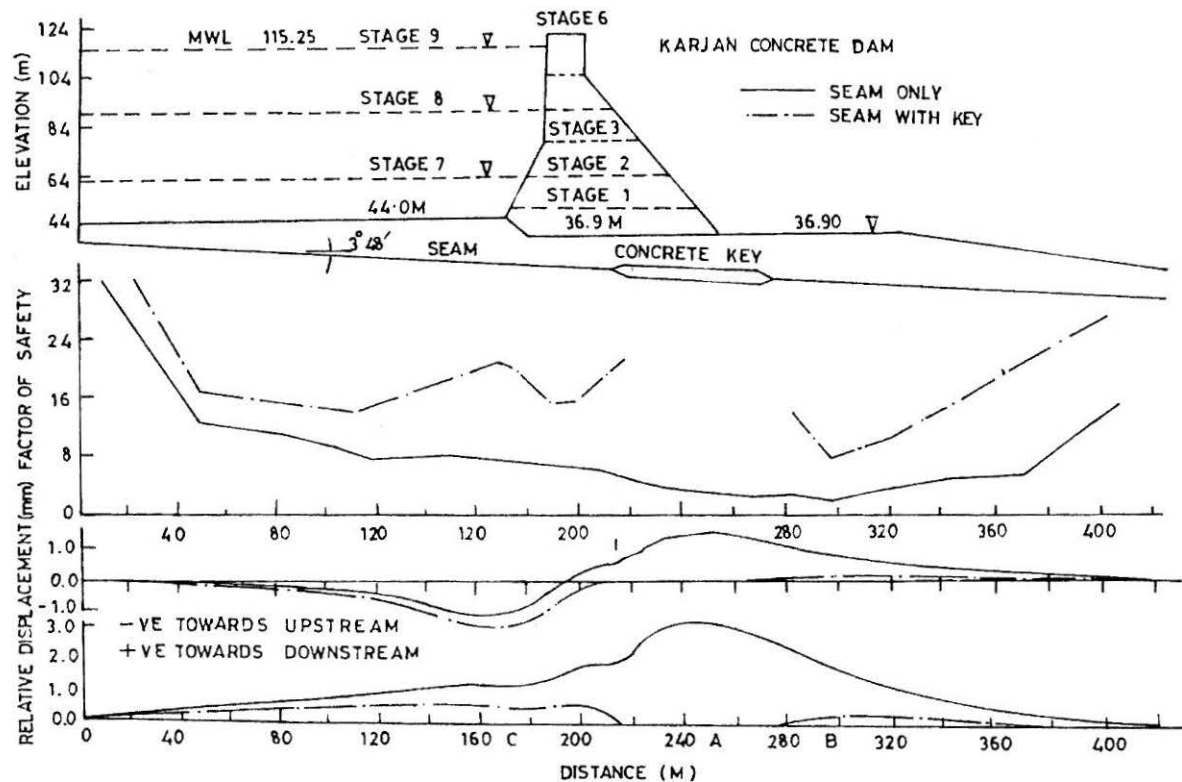


FIGURE 39 : Karjan Dam Foundation

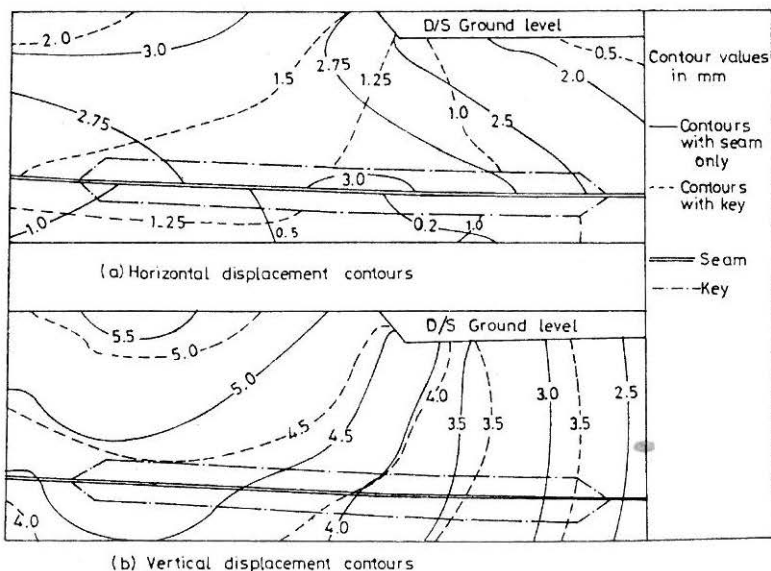


FIGURE 40 : Horizontal and Vertical Displacement Contours

Reinforced Embankment Foundation

Soft clay deposits do not often have adequate shear strength to support embankments. A geosynthetic reinforcement in sheet or grid form is placed on the foundation soil before an embankment is constructed over it. The development of shear stress at the soil reinforcement interface and the tension in the reinforcement provide resistance to failure, thus improving the stability of the embankment foundation system. The mechanism of load sharing and/or transfer among different

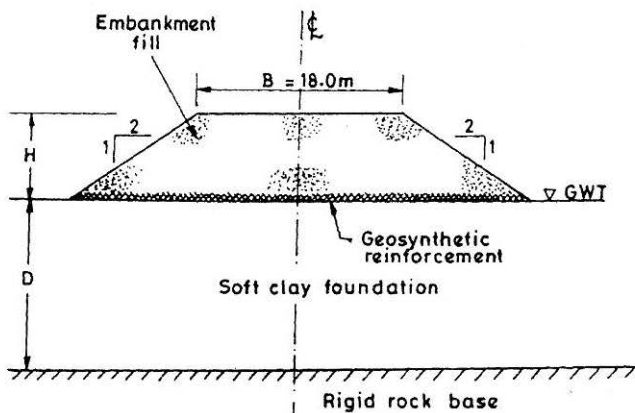


FIGURE 41 : Reinforced Embankment Foundation System

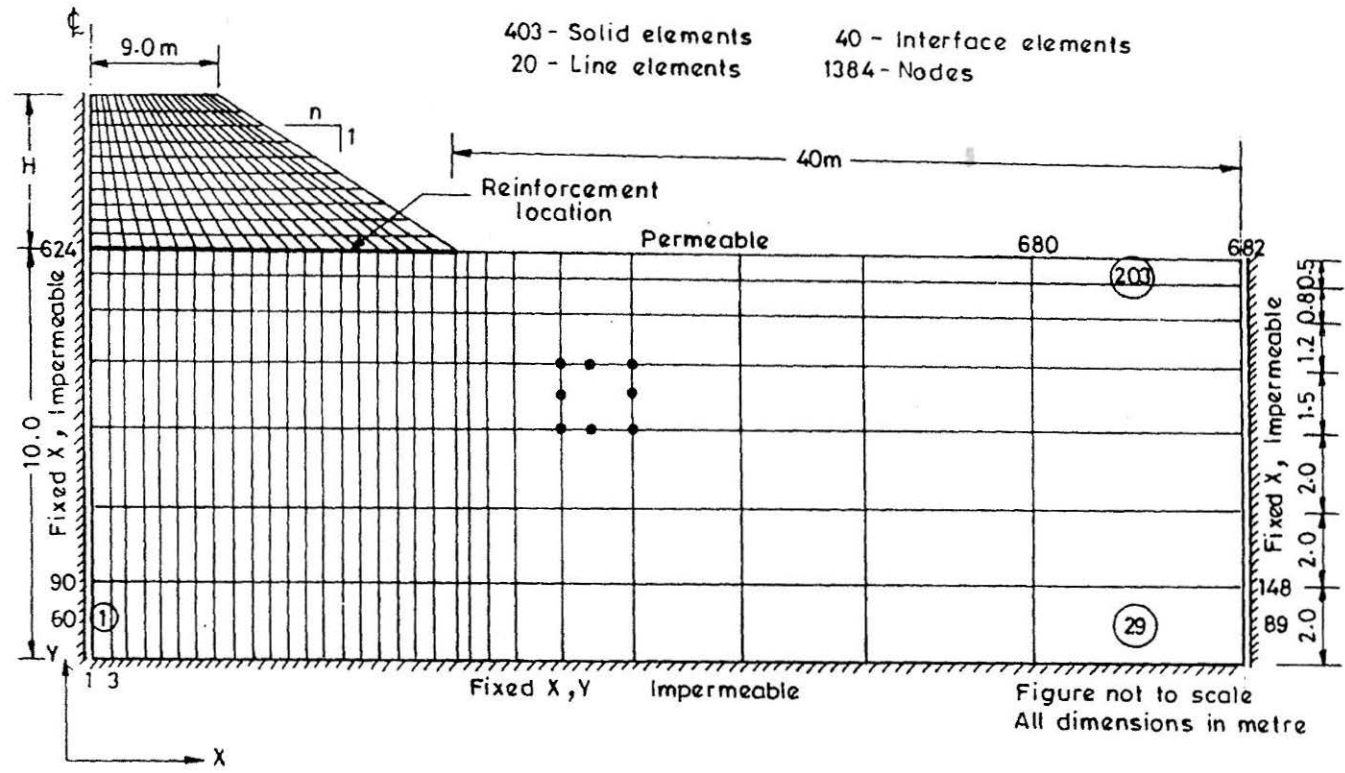


FIGURE 42 : Discretisation of Reinforced Embankment Foundation System

elements, viz., embankment and foundation is complex and is influenced by the properties of the individual elements as well as relative magnitudes of the properties with respect to each other. Conventional methods based on limit equilibrium are inadequate to include these factors. A finite element analysis was conducted to investigate the effects of the type of reinforcement, the depth of foundation and the drainage condition (Aly, 1995; Varadarajan et. al., 1999).

A typical highway embankment of 18 m crest width and 1:2 side slope chosen for the study is shown in Fig.41. The embankment of height, H rests on a soft clay foundation of depth D underlain by a rigid rock deposit. A single layer of geotextile reinforcement was used at the interface between the embankment and the clay foundation.

The discretisation of the reinforced embankment foundation along with the boundary conditions is shown in Fig.42. Three types of elements, (i)

**TABLE 7 : Properties and Strength Parameters used for
Embankment fill Material and Clay Foundation**

Material	Properties used in the analysis
Embankment fill	Unit weight, $\gamma_f = 20 \text{ kN/m}^3$ Cohesion, $c_f = 0$ Angle of internal friction, $\phi_f = 40^\circ$ Janbu's parameter, $K = 150$ Janbu's parameter, $n = 0.5$ Poissons ration, $\nu_f = 0.35$
Clay foundation	Kerala Clay
Submerged unit weight	$\gamma' = 4 \text{ kN/m}^3$
Angle of internal friction	$\phi' = 29^\circ$
Initial void ratio	$e_0 = 3.92$
Compressibility Index	$\lambda = 0.83$
Swelling index	$\kappa = 0.13$
Young's modulus	$E' = 3500 \text{ kP}_a$
Poissons ratio	$\nu' = 0.3$
In situ Stress ratio	$K_0 = 0.52$
Preconsolidation pressure	$P_{c0} = 40 \text{ kP}_a$
Apparent bulk modulus	For undrained analysis $K_a = 3.5 \times 10^5 \text{ kP}_a$
Permeability in vertical direction	For coupled consolidation analysis $k_v = 2 \times 10^{-5} \text{ m/day}$
Permeability in horizontal direction	$k_h = 3 \times 10^{-5} \text{ m/day}$

TABLE 8 : Properties and Strength Parameters used for Interface Elements and Reinforcement

Material		Properties used in the Analysis
Fill-reinforcement interface	Adhesion	$C_a = 0$
	Interface friction angle	$\delta_f = \phi_f = 40^\circ$
	Shear Stiffness	$K_s = 2000 \text{ kN/m}^3$
	Normal Stiffness	$K_n = 3 \times 10^6 \text{ kN/m}^3$
Clay-reinforcement interface (Clay I)	Adhesion	$C_a = C_{uc} = 4.8 \text{ kPa}$
	Interface friction angle	$\delta_f = 0$
	Shear - stiffness	$K_s = 2000 \text{ kN/m}^3$
	Normal stiffness	$K_n = 3 \times 10^6 \text{ kN/m}^3$
Reinforcement	Stiffness J (kN/m)	200, 1000, 2000, 4000, 8000

eight-noded quadrilateral solid elements for the soil, (ii) zero thickness six-noded joint elements for the reinforcement interfaces and (iii) three-noded bar elements for the reinforcement were used.

The clay foundation consisted of clay found in coastal area of Kerala State. The clay had natural water content, 99 to 145%; Liquid Limit, 104 to 105%; Plastic Limit, 31 to 48% and Organic Content, 0.2 to 0.87%. The clay foundation was modelled as an elasto-plastic modified cam-clay model. The behaviour of the embankment fill consisting of sandy soil was represented by an elastic-perfectly plastic material with Mohr-Coulomb yield criterion and fully non-associative flow rule. The Young's modulus of the fill was dependent on stress proposed by Janbu (1963). The geosynthetic reinforcement was characterised with elasto-plastic behaviour using von Mises yield criterion. For interface behaviour between the soil, the Mohr-Coulomb criterion was adopted. The material parameters used are given in Table 7 and 8.

Analyses were conducted to study the effect of the type of reinforcement, the depth of the foundation and the drainage condition. Three foundation depths viz. 2.5, 6 and 10 m were used. The variation of the properties for the reinforcement was chosen based on the data available in literature. The values of the stiffness of the reinforcement chosen were 200, 1000, 2000, 4000 and 8000 kN/m. The coupling of the stress-deformation analysis with consolidation was formulated using Biot's theory to study the effect of the partial drainage condition. For each embankment-foundation configuration, maximum embankment height H_0 without reinforcement was determined and was used as a common datum to compare the effect of

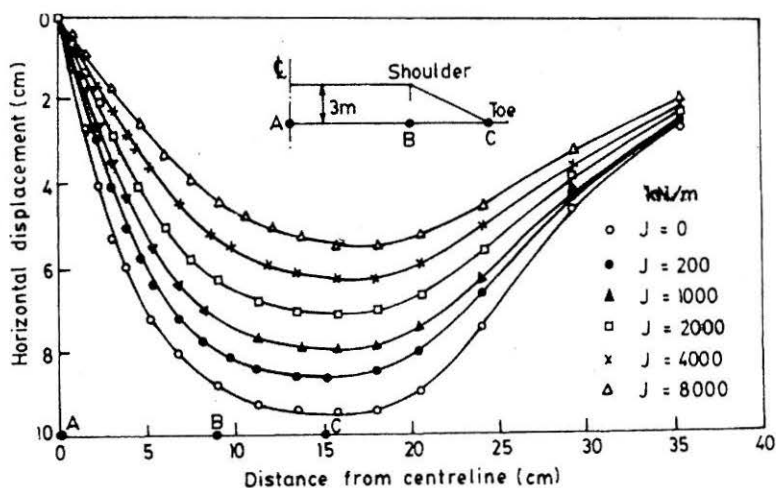


FIGURE 43 : Variation of Horizontal Displacement of the Foundation Surface for Various Reinforcements at $H_0 = 3 \text{ m}$

reinforcement, foundation depth and drainage condition.

Figures 43 and 44 show the effect of the stiffness of the reinforcement on the variation of horizontal and vertical displacement. It is observed that the deformation of foundation surface decreases with the increase in reinforcement stiffness. The maximum effect of reinforcement on the

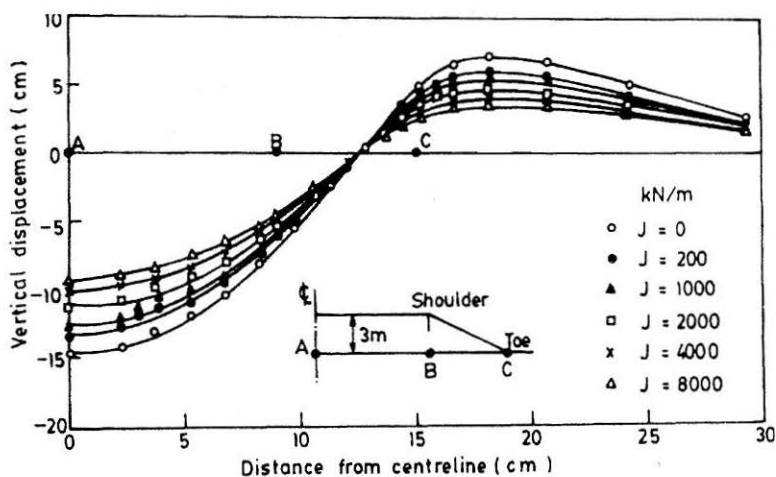


FIGURE 44 Variation of Vertical Displacement of the Foundation Surface for Various Displacements at $H_0 = 3 \text{ m}$

horizontal displacement is noted near the embankment toe whereas the maximum effect on vertical displacement is at the centerline and away from the toe.

The maximum embankment heights H_0 were found to be 3.8, 3.2 and 3 m for the foundation depths 2.5, 6.0 and 10 m respectively. The variations of horizontal and vertical displacements for the three foundation depths are shown in Figs.45 and 46. It is observed that the effect of reinforcement increases with the decrease in the depth of the foundation depth.

The effect of drainage was studied for conducting the analysis under undrained, fully drained and partially drained conditions. For partially drained condition, a time period of 24 days was considered and that was the time chosen for construction of the embankment.

Figures 47 and 48 show the variation of horizontal and vertical displacements on the foundation for the three drainage conditions. It is noted that the undrained condition gives maximum horizontal displacement and minimum vertical displacement. The reverse condition is observed for drained condition.

Underground Structure

For this study, Nathpa-Jhakri Hydropower Project constructed in the

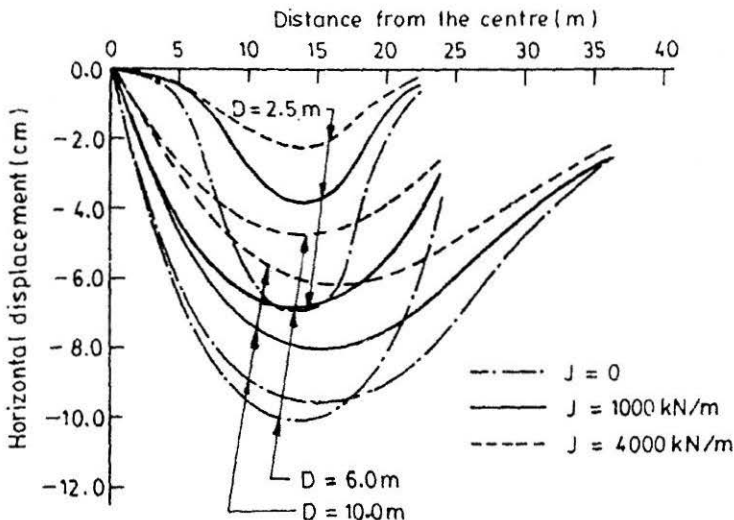


FIGURE 45 : Variation of Horizontal Displacement of Foundation Surface for Various Foundation Depths at H_0

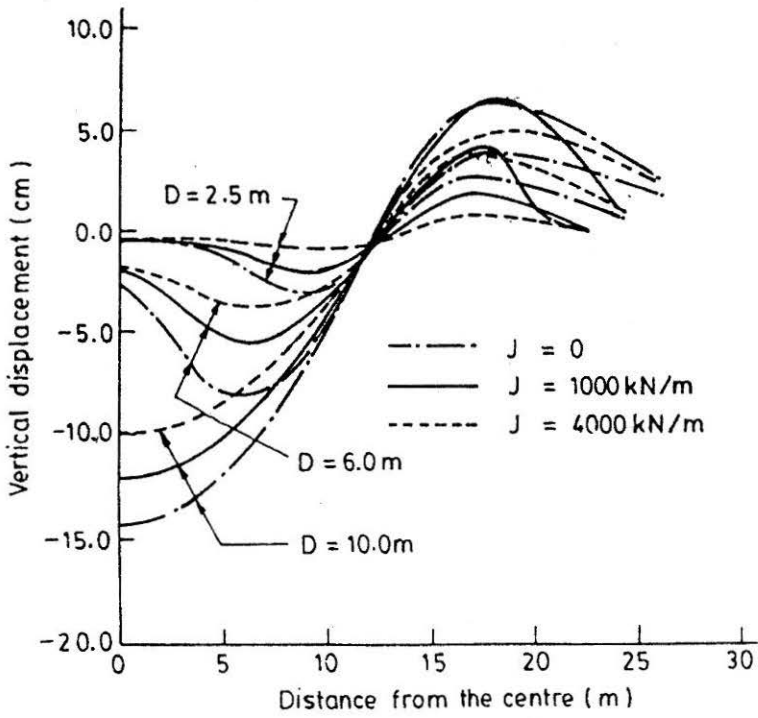


FIGURE 46 : Variation of Vertical Displacement of Foundation Surface for Various Foundation Depths at H_0

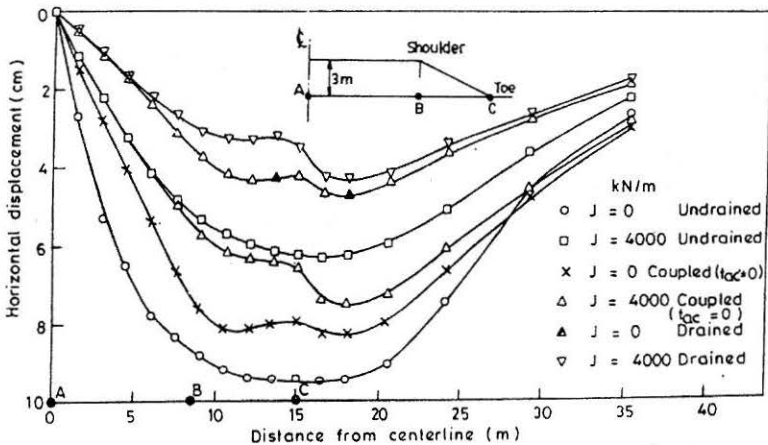


FIGURE 47 : Variation of Horizontal Displacement of Foundation Surface for Various Drainage Conditions

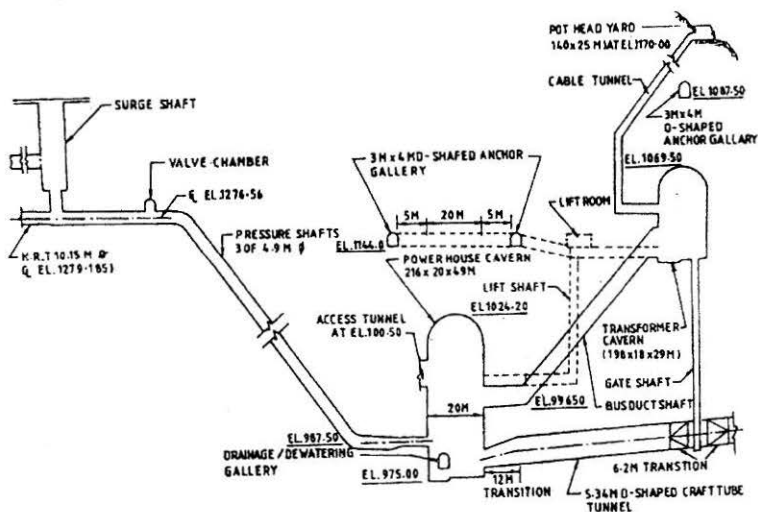


FIGURE 50 : East-West Section of Surge Shaft, Pressure Shaft and Power House Cavern, Nathpa-Jhakri Hydropower Project

(Fig.49), (Hashemi, 1999; Varadarajan et. al., 2001). The power house complex of the project consisted of two major openings, machine hall 216 m × 20 m × 49 m (length × width × height) with an overburden of 262.5 m at crown and the transformer hall 198 m × 18 m × 29 m which was located downstream of machine hall (Fig.50). The rock in the site was

TABLE 9 : Material Parameters for Jointed Rock Mass (Quartz Mica Schist)

Elasticity	ν_j	0.2
	E_j	6677
Ultimate	γ	0.01352
	β	0.3889
Phase Change	n	5.0
Hardening	a_1	0.013E-12
	η_1	0.6
Bonding Stress	3R	41.9
Disturbance	D_u	0.97
	A	220.71
	Z	1.339

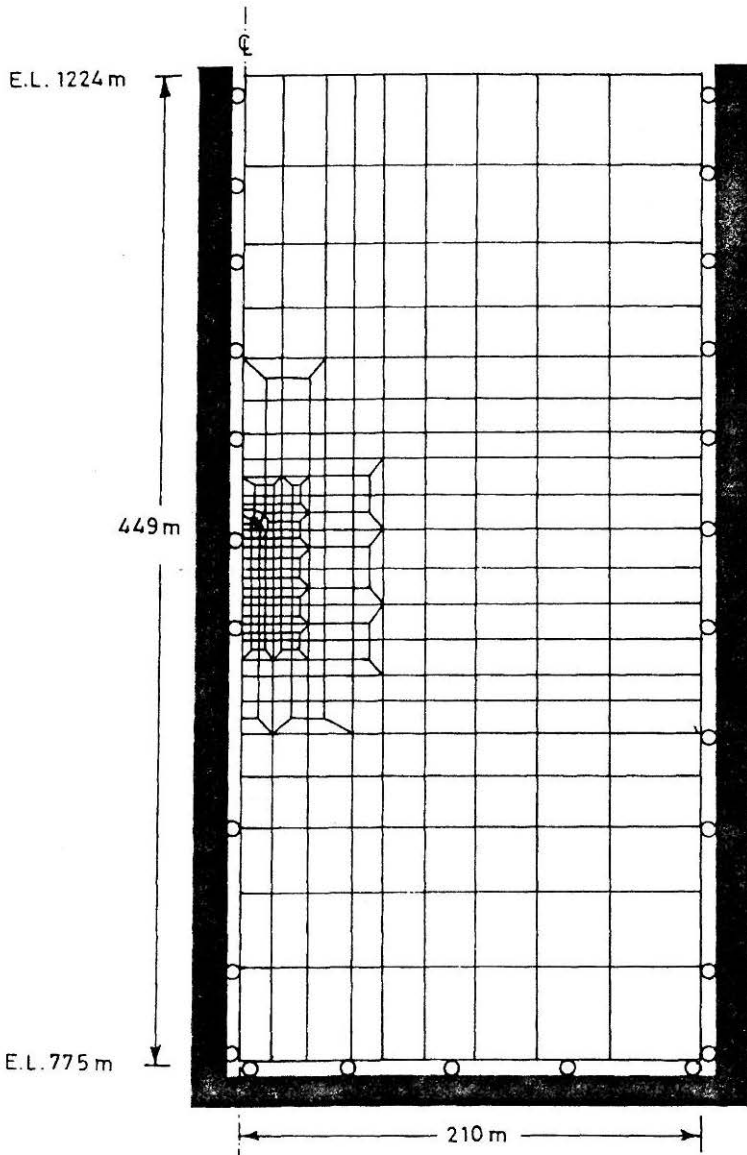


FIGURE 51 : The Discretisation of Carven and Rock Mass

primarily quartz mica schist. The in-situ stress was determined as 5.89 MPa in the vertical direction and 4.73 MPa in the horizontal direction.

The constitutive model based on disturbed state concept (Desai, 1995, 2001) was used to characterise the behaviour of quartz mica schist. The material parameters for the rock mass have to be determined to conduct the finite element analysis. At present, there is no known method which is available to determine the material parameters for the rock mass. For this purpose the procedure suggested by Ramamurthy (1993) to determine the strength and the Young's modulus of the jointed rock mass from the intact properties was extended to determine the material parameters for the constitutive model based on DSC. The material parameters thus obtained are presented in Table 9. The unit weight of the rock mass was 27 kN/m^3 .

The finite element analysis of the machine hall was conducted for the loading due to excavation. The finite element discretisation is shown in Fig.51. The analysis consisted of the simulation of excavation of the cavern in twelve stages of excavation (Fig.52). The computer code DSC-SST-2D developed by Desai (1997) was used. The results of the analysis were processed through a commercial package NISA and the contours of the deformed shape and the variation of major and minor principal stresses around the cavern were plotted for the full excavation of the cavern at 12th stage.

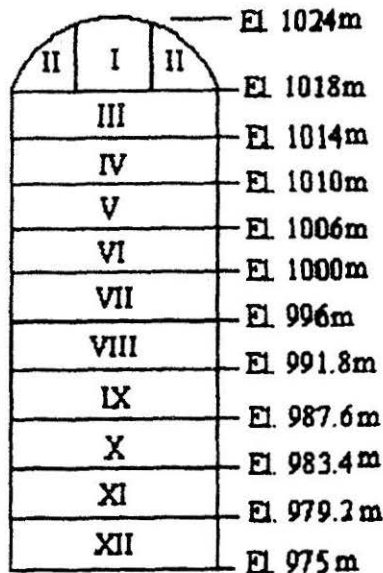


FIGURE 52 : Excavation Sequence for the Power House Cavern

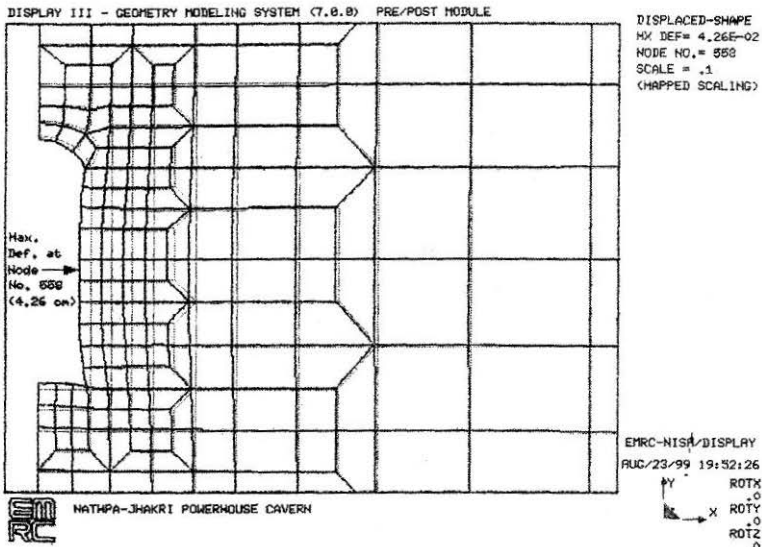


FIGURE 53 : Deformed Shape of the Cavern and Rock Mass

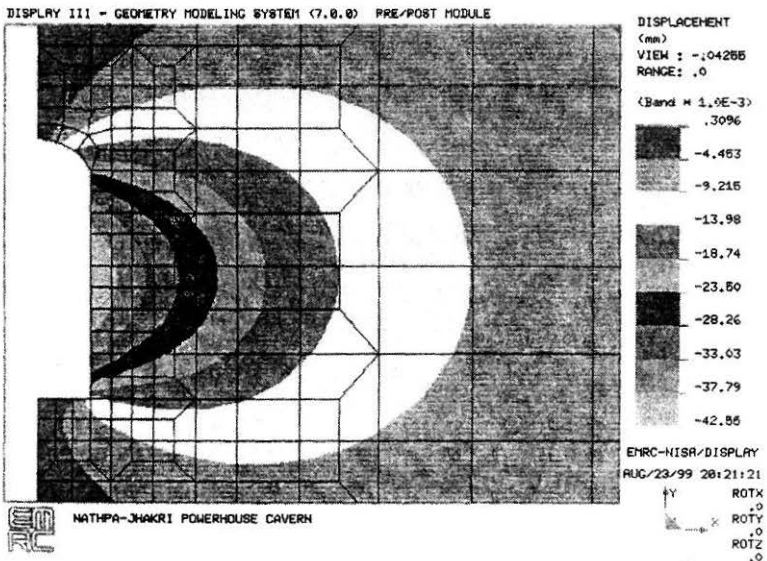


FIGURE 54 : Contours of the Horizontal Displacement
 Around the Cavern

The deformed shape of the cavern of the rock mass is shown in Fig.53. Higher movements of the wall are noted around the mid height of the wall. The maximum value of 42.6 mm is observed at the cavern face and this value decreases to 9.22 mm at a distance of 73 m from the face.

The vertical displacement contours are presented in Fig.54. The maximum upward movement is 24.2 mm at the invert and it reduces to a value of 7.77 mm at a depth of 18.5 m below the invert. At the crown, the maximum downward movement is 12.68 mm and the value decreased to 4.50 mm at a height of 16 m above the crown. The higher vertical movement at the invert portion may be attributed to the large release in-situ stress and also the flat geometry of the invert.

The comparison of the predicted (FEM) and observed (by instrumentation) deformation at the powerhouse cavern boundary is shown in Table 10 (Varadarajan et al., 2001). The predicted values lie within the range of the observed values of the displacements at five out of six locations. It can be considered that, in general, the predictions are satisfactory.

Concluding Remarks

The behaviour of a few geologic materials has been depicted using elastic hyperbolic model, elastoplastic hierarchical single surface model and elastoplastic model based on disturbed state concept. Geologic materials, clay, sand, reinforced sand, rock salt, rock-fill material and rock were tested. Laboratory tests were conducted using a wide range of equipments such as stress-controlled triaxial testing equipment, computer controlled triaxial

TABLE 10 : Comparison of Predicted (FEM) and Observed (instrumentation) Deformation at the Powerhouse Cavern Boundary

StageNo.	Excavation Done		Instrumentation at El. (m)	Deformation (mm)	
	From El. (m)	To El. (m)		Predicted (FEM)	Observed (Instrumentation)
1.	Widening of the Central drift		1024	10.4	13 to 18
2.	Widening of the Central drift		1022	12	6 to 12
3.	1018	1006	1022	0.6	-1.3 to +2.5
4.	1006	1000	1018	3.5	1 to 4
5.	1000	975	1006	23.7	10 to 45
6.		975	996	9.4	1 to 3

equipment, cubical (multiaxial) equipment, high pressure large size triaxial equipment and servo-controlled high pressure triaxial equipment. Material parameters were determined from the tests and the models were verified. The models used were found to provide satisfactory predictions.

Finite element analyses were conducted to study a few problems such as soil-structure interaction problems, foundation of dams, reinforced embankments and underground structure. Constitutive models based on elastic, elasto-plastic and softening theories were incorporated in the analysis. The predictions were compared with observed results in certain cases.

The testing procedures, modeling techniques and analysis methods presented herein indicate a glimpse of recent developments in Geotechnical engineering. The use of these advances, it is believed, will lead to realistic, safe and economic design of structures in Geotechnical Engineering.

Acknowledgements

IIT Delhi has provided the opportunity and support to pursue the research work presented.

Most of the research work has been conducted in close collaboration with the author's colleague Prof. K.G. Sharma. The research work presented here have been primarily drawn from the research work of the former research scholars Dr. K.R. Arora, Dr. S.S. Mishra, Dr. M.A.A. Aly, Dr. K.M. Soñi, Dr. M. Hashmi and Dr. A.K. Gupta. A large part of the research work related to constitutive models is due to the long and continued association of the author with Prof. C.S. Desai, University of Arizona, USA since author's tenure as a Visiting Professor at University of Arizona, Tucson, USA and subsequently under US-India Co-operative Project between IIT Delhi and The University of Arizona, Tucson, USA supported by International Program, National Science Foundation, Washington, D.C. USA.

The research work on Rock-fill Materials was partly supported by the Research Project on Testing and Constitutive Modeling of Rock-fill Materials by Central Soil and Materials Research Station, New Delhi (Ministry of Water Resources).

The author has great appreciation of the understanding and environment provided by his senior colleagues Prof. T. Ramamurthy and Prof. S.K. Gulhati and other colleagues Prof. G.V. Rao, Dr. R. Kaniraj, Dr. K.K. Gupta, Dr. J.M. Kate, Prof. Manoj Datta and Dr. G.V. Ramana.

References

- ALY, M.A.A. (1995) : "Some Aspects of the Behaviour of Reinforced Highway Embankments on Soft Clay", *Ph.D. Thesis*, IIT, Delhi.
- ARORA, K.R. (1980) : "Soil Structure Interaction Analysis of the Strip and Circular Footings on Sand", *Ph.D. Thesis*, IIT Delhi.
- ARORA, K.R. and VARADARAJAN, A. (1984) : "Experimental Investigation on Soil-Structure Interaction of Circular Footings on Sand", *Indian Geotechnical Journal*, 14(2), 127-141.
- BOROWICKA, A. (1936) : "Influence of Rigidity of a Circular Foundation Slab on the Distribution of Pressure over Contact Surface", *Proc. First Int. Conf. Soil Mech. Fund. Engg.*, Cambridge, Mass, 2 : 144-149.
- DESAI, C.S. (1995) : "Constitutive Modeling using the Disturbed State as Microstructure Self-Adjustment Concept", *Chapter 8 in Continuum Models for Materials with Microstructure*, H.B. Muhlhaus (Editor), John Wiley, U.K.
- DESAI, C.S. (2001) : *Mechanics of Materials and Interfaces : The Disturbed State Concept*, CRC Press, Boca Raton, FL, USA.
- DESAI, C.S. AND ABEL, J.F. (1972) : *Introduction to the Finite Element Method*, Van Nostrand Reinhold Co. New York, U.S.A.
- DESAI, C.S. and WATHUGALA, G.W. (1987) : "Hierarchical and Unified Models for Solids and Discontinuities (Joints / Interfaces)", *Short Course Notes*, 2nd International Conference on Const. Laws for Engineering, Mater : Theory and Applications, Tucson, Arizona, USA.
- DESAI, C.S. and VARADARAJAN, A. (1987) : "A Constitutive Model for Short Term Behaviour of Rock Salt", *Journal of Geophysical Research*, Oct.
- DESAI, C.S., SOMASUNDARAN, S. and FRANTZISKONIS, (1986) : "A Hierarchical Approach for Constitutive Modeling of Geologic Materials", *Int. J. Numer. Anal. Meth Geomech.*, 10(3).
- GUPTA, A.K. (2000) : "Constitutive Modeling of Rock-fill Materials", *Ph.D. Thesis*, IIT Delhi.
- HASHEMI, M. (1999) : "Constitutive Modeling of a Schistose Rock in the Himalayas", *Ph.D., Thesis*, IIT Delhi.
- JANBU, N. (1963) : "Soil Compressibility as Determined by Oedometer and Triaxial Tests", *European Conference Soil Mechanics and Foundation Engineering*, Wiesbaden, Germany, 1, 19-25.
- KONDNER, R.L. and ZELASKO, J.S. (1963) : "Void Ratio Effects on Hyperbolic Stress-Strain Response of a Sand", *Laboratory Shear Testing of Soils*, ASTM, STP No.361.
- LOWE, J. (1964) : "Shear Strength of Coarse Embankment Dam Materials", *Proc. 8th Intl. Congress in Large Dams*, 3, 745-761.
- MISHRA, S.S. (1981) : "Effect of Stress-Path on the Stress-Strain-Volume Change Behaviour of Some Granular soils", *Ph.D. Thesis*, IIT Delhi.

RAMAMURTHY, T. (1993) : "Strength and Modulus Responses of Anisotropic Rocks", *Chapter 13 in Comprehensive Rock Engineering, Vol. I*, Pergamon Press, Oxford, U.K.

ROSCOE, K.H. (1970) : "The Influence of Strains in Soil Mechanics", *Geotechnique*, 20(2), 129-170.

SONI, K.M. (1995) : "Constitutive Modeling of Reinforced Soil", *Ph.D. Thesis*, IIT Delhi.

TAYLOR, D.W. (1970) : *Fundamentals of Soil Mechanics*, John Wiley & Sons, New York.

TERZAGLIN, K. and PECK, R.B. (1968) : *Soil Mechanics in Engineering Practice*, John Wiley & Sons, Inc. New York.

VARADARAJAN, A. (1973) : "Effect of Over-consolidation and Stress-Path on Saturated Remoulded Clays during Shear", *Ph.D. Thesis*, IIT Kanpur.

VARADARAJAN, A. and ARORA, K.R. (1979) : "An Interaction Study of Strip-Footing – Sand – Bed System by Finite Element Method", *Proc. Third Int. Conf. on Numerical Methods in Geomechanics*, 1041-1051.

VARADARAJAN A. and ARORA, K.R. (1982) : "Interaction of Circular Footings-Sand Bed System", *Proc. Fourth Int. Cong. on Numerical Methods in Geomechanics*, Edmonton, 945-953.

VARADARAJAN, A. and SHARMA, K.G. (1989) : "Effect of Shear Seam in the Foundation of Karjan Dam", *Int. Jl. For Numerical Anal. Meth Geomech.*, 13, 435-442.

VARADARAJAN, A., SHARMA, K.G. and SONI, K.M. (1999) : "Constitutive Modeling of A Reinforced Soil using Hierarchical Model", *Int. Jl. Num. Anal. Methods in Geomech.*, 23, 217-241.

VARADARAJAN, A., SHARMA, K.G. and ALY, M.A.A. (1999) : "Finite Element Analysis of Reinforced Embankment Foundations", *Int. Journal For Numer. Anal. Meth. Geomech.*, 23, 103-114.

VARADARAJAN, A., SHARMA, K.G., DESAI, C.S. and HASHEMI, M. (2001) : "Constitutive Modeling of Schistose Rock in the Himalayas", *The Int. J. of Geomechanics*, 1(1), 83-107.

VARADARAJAN, A., SHARMA, K.G., DESAI, C.S. and HASHEMI, M (2001) : "Analysis of a Power House Cavern in the Himalayas. *The Int. J. of Geomechanics*, 1(1), 109-127.

VARADARAJAN, A., SHARMA K.G., VENKATACHALAM, K and GUPTA, A.K. (2001) : "Testing and Modeling of Two Rock-fill Materials", *Journal of Geotechnical and Geoenvironmental Engg.*, ASCE, Tentative Acceptance.

YUDHBIR and VARADARAJAN, A. (1975) : "Stress-Path Dependent Deformation Modulus of Clay", *Jl. of Geotechnical, Engg. Div.*, ASCE. 101, GT3, 315-327.

YUDHBIR and VARADARAJAN, A. (1974) : "Lateral Earth Pressure Analysis using Relevant Soil Modulus", *Technical Note, Soils and Foundations*, 14(2), 90-95.